Kempf et al. *Swiss Journal of Geosciences* (2022) 115:14
https://doi.org/10.1186/s00015-022-00415-y

SGG SGS sc | nat
Swiss Journal of Geosciences

ORIGINAL PAPER Open Access

Serpentinite dehydration at low pressures

Elias D. Kempf[1*], Jörg Hermann[1] and James A. D. Connolly[2]

Abstract

Petrographic observations combined with mineral compositional analyses constrain the phase relations of prograde metamorphosed serpentinites in the Bergell contact aureole (Italy). In a 1500 m profile perpendicular to the north-eastern edge of the Bergell intrusion, seven dehydration reactions ran to completion. Three previously undocumented reactions have been identified within 70 m of the intrusive contact: olivine + anthophyllite = orthopyroxene + H_2O, tremolite + Cr–Al-spinel = olivine + Mg-hornblende + H_2O and chlorite = olivine + orthopyroxene + Cr-Al-spinel + H_2O. Petrological analysis indicates that these reactions occur over a narrow range of pressure and temperature, 300 ± 30 MPa and 720 ± 10 °C respectively. Computed phase diagram sections reproduce the observed mineral parageneses with one notable exception. Due to the underestimation of aluminium and sodium contents in Ca-amphibole models, plagioclase is predicted above 700 °C instead of Mg-hornblende. In comparison with natural grains, the aluminium content of computed chlorite compositions is overestimated for low grade parageneses while it is underestimated near the upper thermal stability limit of chlorite. In the computed sections, Fe partitioning relative to Mg between olivine and other silicates, suggests a clear preference for Fe in olivine, that therefore shows lower Mg#s. In contrast, microprobe analyses of natural mineral pairs indicate that orthopyroxene, Mg-hornblende and anthophyllite have lower Mg#s than equilibrium olivine. The inferred thermal profile of the metamorphic aureole is not consistent with simple heat conduction models and indicates a contact temperature of ~ 800 °C, which is 120–230 °C higher than previously estimated. Petrography also reveals extensive retrograde overprint of the prograde parageneses within 200 m of the contact. Retrogression is related to metamorphic fluids that were released by dehydration reactions during contact metamorphism and magmatic fluids expelled from the tonalite intrusion. The thermal gradient between the intrusion and the country rocks induced hydrothermal circulation of these fluids throughout the contact aureole, which beyond peak metamorphic conditions caused retrograde overprint of the prograde parageneses. The proposed phase relations for low and high pressures, and in particular, the transition from tremolite to Mg-hornblende, provides a complete representation of hydration and dehydration processes in serpentinites in subduction zones, along deep oceanic transform faults, and at passive continental margins. The latter has new implications, specifically for subduction initiation.

Keywords: Contact metamorphism, Serpentinites, Fe–Mg partitioning, Mg-hornblende, Chlorite, Spinel, Plagioclase, Olivine, Phase relations, Subduction initiation

1 Introduction

Contact metamorphic aureoles are natural laboratories that provide constraints on metamorphic processes (Eskola 1914, 1921; Goldschmidt 1911, 1922; Kerrick 1991; Tracy & Frost 1991). They form under approximately eustatic conditions in the country rocks surrounding magmatic intrusions. Metamorphic temperatures in the aureole increase continuously with decreasing distance from the intrusive body, providing excellent control on prograde mineral parageneses. Therefore, in contact aureoles with large continuous lithologies, mapping of isograds is possible.

At Valmalenco, northern Italy, a classic and accessible contact metamorphic aureole is exposed where the

Editorial handling: Edwin Gnos.

*Correspondence: elias.kempf@geo.unibe.ch
[1] Institute of Geological Sciences, University of Bern, Baltzerstrasse 1+3, CH-3012 Bern, Switzerland
Full list of author information is available at the end of the article

Springer Open

© The Author(s) 2022. **Open Access** This article is licensed under a Creative Commons Attribution 4.0 International License, which permits use, sharing, adaptation, distribution and reproduction in any medium or format, as long as you give appropriate credit to the original author(s) and the source, provide a link to the Creative Commons licence, and indicate if changes were made. The images or other third party material in this article are included in the article's Creative Commons licence, unless indicated otherwise in a credit line to the material. If material is not included in the article's Creative Commons licence and your intended use is not permitted by statutory regulation or exceeds the permitted use, you will need to obtain permission directly from the copyright holder. To view a copy of this licence, visit http://creativecommons.org/licenses/by/4.0/.

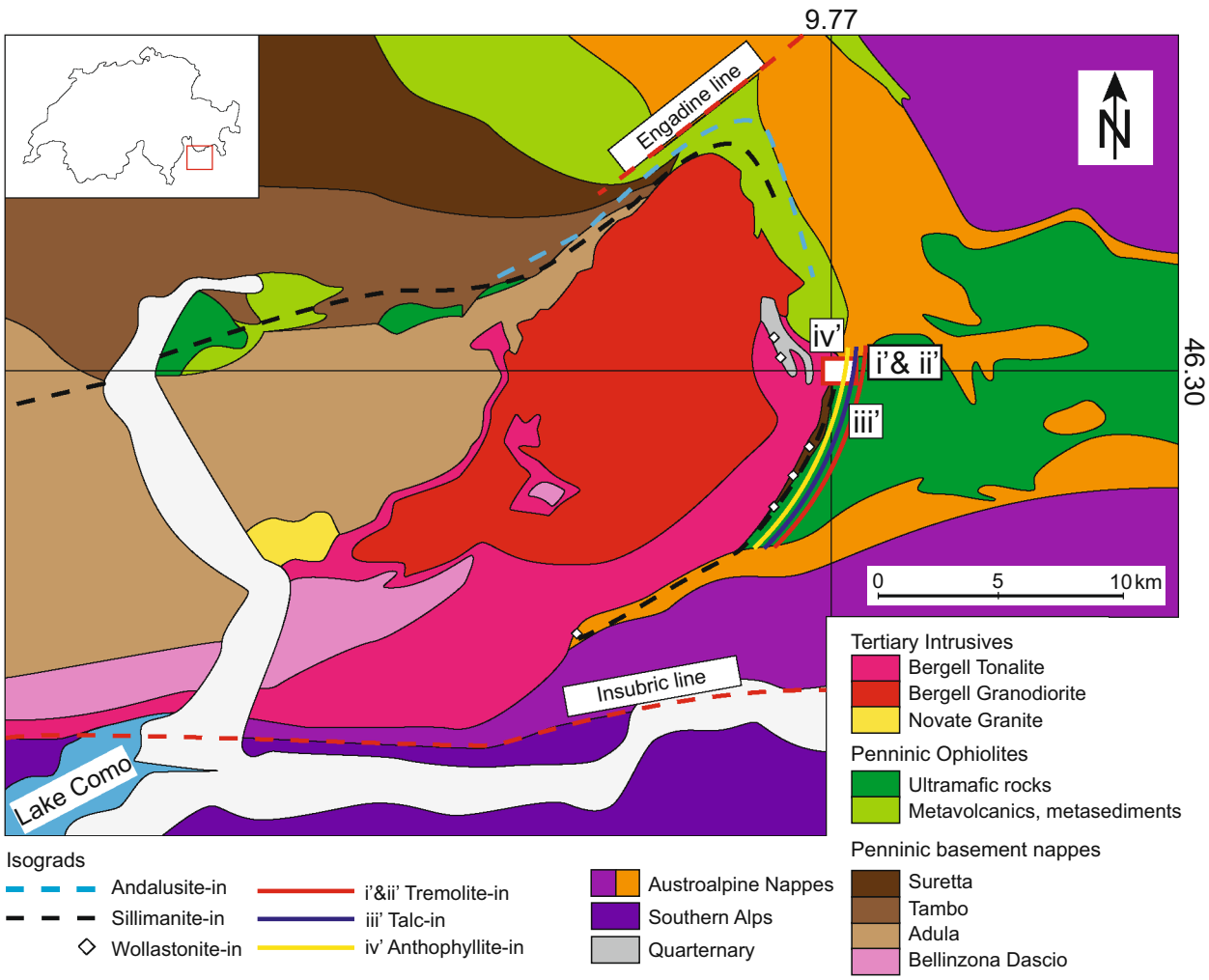

Fig. 1 The geologic setting of the Bergell intrusion between the upper Engadine valley (Switzerland) and the Valtellina (Italy) modified from Wenk and Cornelius (1977) and Trommsdorff et al. (2005). Isograds are after Trümpy and Trommsdorff (1980). The study area is outlined with the red rectangle (coordinates are given in WGS 84)

Bergell tonalite and granodiorite melts intruded into greenschist facies country rocks at upper crustal levels (Fig. 1). The aureole is most reknown for phase relation studies in the Malenco serpentinites (Trommsdorff & Evans 1972) including its ophicarbonates (Eberhard & Pettke 2021; Pozzorini 1996; Trommsdorff & Evans 1977) but also mesozoic sediments (Bucher-Nurminen 1977; Gieré 1985; Trommsdorff & Schwander 1969; Wenk et al. 1974), metabasalts (Riklin 1978) and basement rocks (Bucher-Nurminen 1977; Gyr 1967). Trommsdorff and Evans (1972) have shown that in the Malenco serpentinites, the pre-intrusive regional paragenesis consists of antigorite, olivine, (chlorite), diopside and magnetite. Through a series of bulk rock measurements, they have also shown that prograde metamorphism in the meta-serpentinites of the Bergell contact aureole is isochemical except for H_2O loss during dehydration. Trommsdorff and Evans (1972) and Trommsdorff and Connolly (1996) defined five prograde parageneses which form characteristic mineral zones towards the pluton representing increasing metamorphic grade; **(I)** olivine + antigorite + tremolite + chlorite + magnetite, **(II)** Ti-clinohumite + olivine + Mg-ilmenite (geikilite), **(III)** olivine + talc + tremolite + chlorite + magnetite, **(IV)** anthophyllite + olivine + tremolite + chlorite + magnetite and **(V)** olivine + enstatite + tremolite + chlorite + magnetite. Based on the changing mineralogy, they defined five reactions corresponding to isograds: **I′** = tremolite-in, **II′** = Ti-clinohumite-out, **III′** = talc-in, **IV′** = anthophyllite-in and **V′** = orthopyroxene-in. Trommsdorff and

Evans (1980) pointed out that zones **I** and **II** coincide throughout the contact aureole defining a combined zone **I&II** and that zone **III** is the most simple to recognize in the field. According to Trommsdorff and Connolly (1996), zone **IV** and **V** parageneses occur only sporadically in the immediate vicinity of the intrusion, implying that isograds **IV′** and **V′** are only defined locally. Assuming a tonalite implacement temperature of 700 °C, they argued that the formation of orthopyroxene occurred due to a reduction in H_2O activity consequent to CO_2 release by decarbonation reactions in neighbouring lithologies. They suggested low contact temperatures of 570 °C based on carbonate thermometry in ophicarbonates, assuming an ambient pressure of 350 MPa in the serpentinites at the time of magma implacement. Ferry (1995) provided an alternative peak metamorphic temperature profile for the Bergell contact aureole. He used an exponential equation which represents temperatures around cooling plutons from Furlong et al. (1991), suggesting higher contact temperatures (680 °C) than Trommsdorff and Connolly.

In this study, we focus on the prograde and retrograde metamorphic reactions in contact metamorphic serpentinites from the north-eastern edge of the aureole which represents the most complete profile in serpentinites towards the Bergell pluton (Fig. 2). We inspect the changing prograde and retrograde parageneses based on micro-textural evidence and compare them with characteristic prograde parageneses reported from other contact aureoles (e.g., Berg & Docka 1983; Evans & Frost 1976; Frost 1975, 1976; Matthes & Knauer 1981; Rice et al. 1974; Robinson et al. 1982; Springer 1974). The petrographic evidence is then linked to chemical changes regarding major and minor element characteristics in key phases such as chlorite, Ca-amphibole and spinel group minerals. Likewise, we re-assess Fe–Mg partitioning data between olivine and paragenetic phases using natural data from this study and from various literature sources (e.g., Padrón-Navarta et al. 2010; Robinson et al. 1982; Trommsdorff & Evans 1972; Trommsdorff et al. 1998). Our observed phase relations combined with reaction curves from the literature (e.g., Chernosky et al. 1985; Evans 1976; Evans & Trommsdorff 1970; Jenkins 1983; Jenkins & Chernosky 1986; Mandler & Grove 2016; Niida & Green 1999; Trommsdorff & Evans 1980; Wang et al. 2020) lead us to propose new phase relations for low pressure meta-serpentinites. We explore the key differences between these phase relations and the computed phase diagram sections. In particular, we focus on the stability of Ca-amphibole versus plagioclase at upper amphibolite conditions in serpentinized peridotites. On the basis of our phase relations, we then revise the thermal profile and contact temperatures of the Bergell aureole and investigate phase relations of chlorite and Ca-amphibole forming reactions over a wide pressure and temperature range. These reactions are relevant to various geodynamic processes. For example, deep hydration processes in the oceanic lithosphere, subduction initiation, subduction infancy and subduction of the oceanic lithosphere.

2 Geological setting

The Malenco-Forno ophiolitic unit in Valmalenco (Northern Italy) and Puschlav (south-eastern Switzerland) is a remnant of the Piedmont-Ligurian oceanic lithosphere (Dietrich 1974). It forms the Penninic-Austroalpine boundary zone between the European and Adriatic continental margins (Trommsdorff et al. 2005). The European crust lies tectonically below the Malenco-Forno unit and is represented by middle penninic basement nappe stacks (Suretta-, Tambo-, Adula-, Bellinzona-Dascio-nappes) including their sedimentary cover (Fig. 1). The Adriatic continental basement nappe stacks (Bernina-, Sella- and Margna-nappes) and their sedimentary cover lie tectonically above the Malenco-Forno unit. The Malenco-Forno unit contains one of the largest serpentinized ultramafic bodies in the Alps (Staub 1921, 1946; Trommsdorff & Evans 1972) and preserves a Permian fossil subcontinental lower crust to mantle transition of the Adriatic micro-continent (Hermann et al. 1997; Müntener & Hermann 1996; Trommsdorff et al. 1993). Serpentinization occurred during Jurassic rifting through seawater infiltration (Burkhard & O'Neil 1988) when locally ophicarbonates were formed (Pozzorini 1996; Trommsdorff & Evans 1977; Trommsdorff et al. 1993). Regional metamorphism overprinted the whole nappe stack at 600–700 MPa and 450–500 °C (Bucher & Pfeifer 1973; Guntli & Liniger 1989; Trommsdorff 1974) and was followed by polyphase deformational overprint (Hermann & Muntener 1992). During the Oligocene, the Bergell tonalite, (32 Ma) hornblende gabbros and later granodiorite (30 Ma) intrusions discordantly crosscut the nappe stacks (Fig. 2), causing contact metamorphic overprint in the surrounding country rocks (Diethelm 1985; Hansmann 1996; Jäger 1973; Reusser 1987; von Blackenburg 1992). At the eastern border, thermal metmorphism produced a 1–1.5 km wide aureole in the mostly lherzolitic and harzburgitic Malenco serpentinites (Trommsdorff & Evans 1972) where the contact with the tonalite is mostly vertical (Trommsdorff & Connolly 1996). The tonalite dips subvertically underneath Monte Disgrazia and at its northern edge with a lower angle underneath the Forno basalts where the aureole is 2.5 km wide (Riklin 1978).

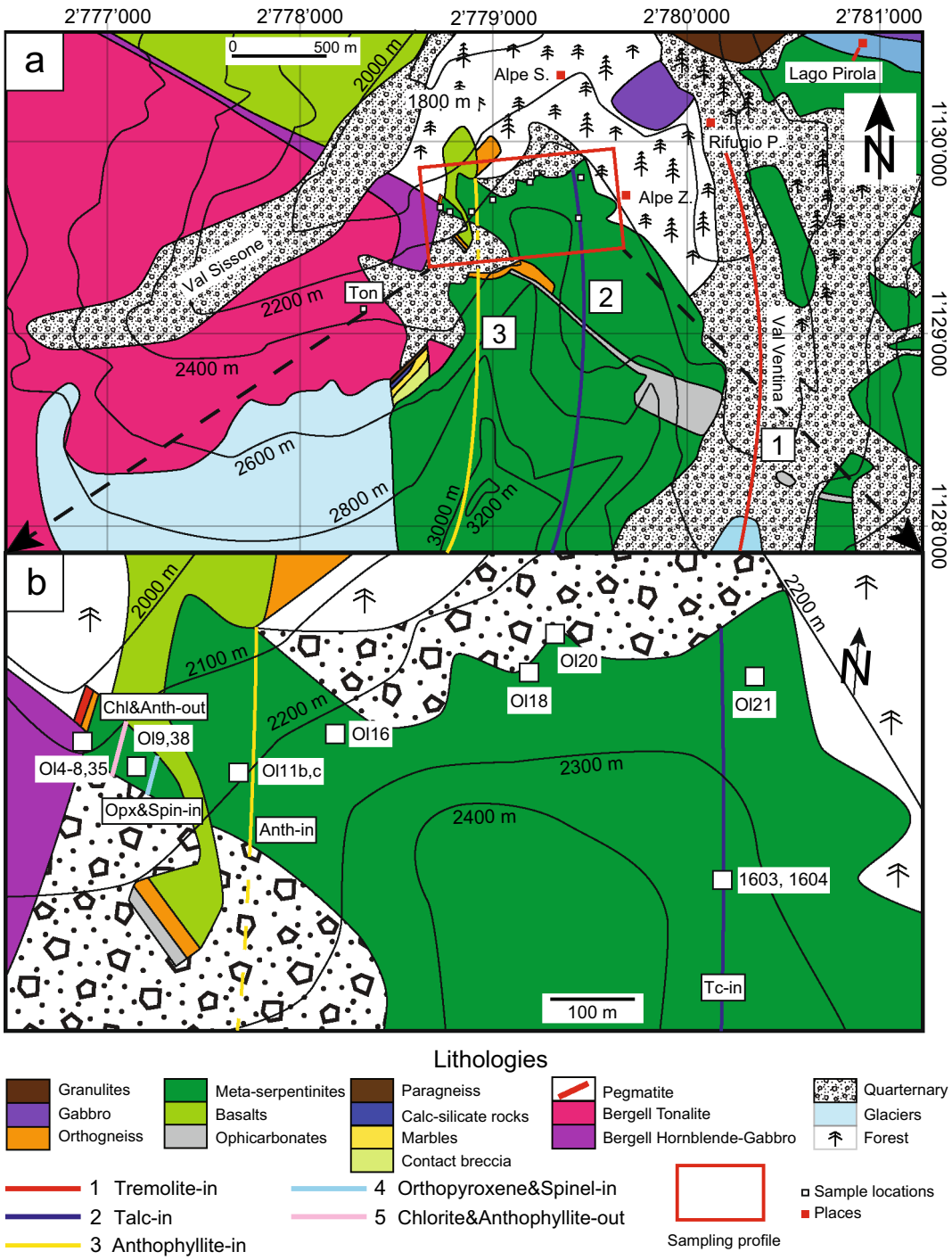

Fig. 2 **a** The geological map of the studied ultramafic rocks modified from Trommsdorff et al. (2005). A detailed sample profile was collected from Val Ventina to Val Sissone (red rectangle). Numbers in the map correspond to the mapped isograds from Trommsdorff and Evans (1972) modified by Trümpy and Trommsdorff (1980) and this study. The coordinate grid is given in Swiss coordinates CH1903 +/LV95. **b** Zoom-in on the sampling profile of **a** with sample location corresponding coordinates presented in Table 1. Contour lines in both **a** and **b** are given in meters above sea-level (m.a.s.l.). Mineral abbreviations are presented in Table 1

3 Methods

Polished thin sections of 30 µm thickness (Table 1) were investigated by optical microscopy, BSE imaging and quantitative WDS analyses.

3.1 Electron probe micro analyser (EPMA)

The JEOL JXA-8200 Superprobe of the Institute of Geological Sciences at the University of Bern was used for quantitative mineral chemistry analyses. The instrument is equipped with five wavelength dispersive crystal spectrometers (WDS) and one energy dispersive spectrometer (EDS). Imaging and micro-textural analyses were performed with a backscatter detector (BSE). Samples were analysed at a 15 kV acceleration voltage and a probe current of 20 nA. The measurement time included 20 s on the peak and 10 s on each background position. These measurement conditions have detection limits of 0.01 wt% (Batanova et al. 2015). All values lower than the detection limit are indicated with "below detection" (b.d.) in the text and tables. Olivine, pyroxene and spinel were analysed under a focused beam, whereas for sheet silicates and amphiboles, a defocused beam of 3–5 µm diameter was used depending on grain size. Natural and synthetic oxides and silicate minerals were used as standards.

3.2 Thermodynamic modelling

Phase diagram sections were calculated for a lherzolitic serpentinite bulk sample lr21 from Li et al. (2004): 41.37 wt% SiO_2, 4.06 wt% Al_2O_3, 0.60 wt% Cr_2O_3, 6.32 wt% FeO, 35.03 wt% MgO, 2.93 wt% CaO and 8.95 wt% H_2O. Since Na_2O was reported to be < 0.05 wt% by the latter authors, we added 0.03 wt% Na_2O in order to test Ca-amphibole model compositions. We used the Perple_X software package of Connolly (2009) and the 2002 revision of the thermodynamic data base of Holland and Powell (1998) augmented with data for Cr-oxide solutions (Klemme et al. 2009). The following solution models from Holland and Powell (1998) were considered including their fluid equation of state: Olivine O(HP), chlorite Chl(HP), orthopyroxene Opx(HP), talc T, brucite B, orthoamphibole from Diener and Powell (2012) oAmph(DP), Ca-amphibole from Dale et al. (2000) GlTrTsPg, antigorite from Padrón-Navarta et al. (2013) Atg(PN) and Cr-Al-spinel from Klemme et al. (2009) CrSp. For comparison, a phase diagram section was calculated with the more recent data base of Holland et al. (2018) using the corresponding solution models: Olivine O(HGP), orthopyroxene Opx(HGP), Al-spinel Sp(HGP), talc (T), brucite (B), chlorite from White et al. (2014) Chl(W), orthoamphibole from Diener and Powell (2012) oAmph(DP), Ca-amphibole from Green et al. (2016) cAmph(G), antigorite from Padrón-Navarta et al. (2013) Atg(PN) and using the fluid equation of state from Pitzer and Sterner (1994). The Mg#s of all phases, the Cr# of Cr–Al-spinel and the Al per formula unit (pfu) for chlorite and Ca-amphibole were then calculated in the system Na_2O–CaO–MgO–FeO–Al_2O_3–Cr_2O_3–SiO_2–H_2O, assuming excess H_2O.

4 Results

Serpentinites originate mostly from lherzolitic protoliths, including samples Ol44, Mal1101, CH2, Ol22, Ol21, Ol20, Ol11b, Ol9, Ol38, Ol6, Ol4 and Ol35. Samples 1603, 1604, Ol16, Ol11c and Ol8 show low diopside or Ca-amphibole content and are therefore harzburgitic. Ol18 is Ca-amphibole rich and may have a pyroxenite protolith. In the following, prograde parageneses defined as zones **O**–**VI** are described in detail. The regional metamorphic zone **O** is presented in Additional file 1: Figure S1 and Additional file 2: File S1. Sample names, sample types, prograde parageneses, metamorphic zones, distance from the contact, sample locations in Swiss coordinates and mineral abbreviations are given in Table 1.

4.1 Prograde mineral parageneses in serpentinites towards the intrusion

4.1.1 Zone I&II (1500–750 m from the contact): first appearance of tremolite

The mineral assemblage of zone **I&II** is olivine, antigorite, tremolite, relic Cr-magnetite, magnetite and antigorite (Fig. 3). At the outcrop scale, zone **I&II** serpentinites show a massive felsic to schistose fabric (see Figs. 2a and b for location and 3a, Sample Ol21). Microscopically, olivine exhibits sub-idioblastic habitus and grain sizes vary between a few tens of microns (Fig. 3b). Antigorite blades define the foliation in schists and show interlocking textures in massive rocks. Tremolite shows an acicular habitus and is a few tens to hundreds of microns long. It often occurs in olivine-rich zones with low antigorite content (Fig. 3b–e), grows oblique to the foliation and occasionally forms aggregates (Fig. 3c and d). Therefore, the prograde paragenesis consists of olivine, tremolite and antigorite. Additionally, two types of spinel group minerals occur. Large relic Cr-magnetites show dark inclusion-rich cores surrounded by inclusion-free rims (Fig. 3e). The rims display grey-scales similar to fine-grained magnetites found in the ground mass and as inclusions in olivine and tremolite. Apart from surface weathering, no retrograde overprint has been observed in zone **I&II** (Sample Ol21).

4.1.2 Zone III (750–200 m from the contact): olivine + talc

The mineral assemblage of zone **III** is olivine, talc, tremolite, chlorite, relic Cr-magnetite, magnetite, antigorite and late serpentine (Fig. 4). At the outcrop scale, the

Table 1 Samples

Sample	Type	Prograde parageneses	Distance to intrusion in meters	Zone	Coordinates CH1903 +/LV95
Mal1101	Schist	Atg, Ol, Di, Chl, Ti-cl, Mt, Cr-Mt	> 1500	O	2′785′790 1′127′825
CH2	Schist	Atg, Ol, Di, Chl, Ti-cl, Mt, Cr-Mt	> 1500	O	2′785′790 1′127′825
Ol22	Vein	Atg, Ol, Di, Chl, Ti-cl, Mt, Cr-Mt	> 1500	O	2′785′790 1′127′825
Ol44	Vein	Atg, Ol, Di, Chl, Ti-cl, Mt, Cr-Mt	> 1500	O	2′780′295 1′129′535
Ol21	Schist	Atg, Ol, Trm, Chl, Mt, Cr-Mt	800	I&II	2′779′421 1′129′998
1603	Vein	Ol, Tc, Trm, Chl, Mt, Cr-Mt	750	III	2′779′440 1′129′583
1604b	Vein	Ol, Tc, Trm, Chl, Mt, Cr-Mt	750	III	2′779′440 1′129′583
Ol20	Fels	Ol, Tc, Trm, Chl, Cr-Mt	540	III	2′779′220 1′129′843
Ol18	Fels	Ol, Tc, Trm, Chl, Cr-Mt	500	III	Close to Ol20
Ol16	Fels	Ol, Tc, Trm, Chl, Cr-Mt	310	III	2′779′000 1′129′706
Ol11b	Fels	Ol, Anth, Trm, Chl, Cr-Mt	190	IV	2′778′876 1′129′635
Ol11c	Fels	Ol, Anth, Trm, Chl, Cr-Mt	170	IV	2′778′845 1′129′628
Ol9, Ol38	Fels	Ol, Opx, Anth, Mg-Hbl, Chl, Cr–Al-Spin	70	V	2′778′759 1′129′622
Ol8	Fels	Ol, Opx, Mg-Hbl, Cr–Al-Spin	35	VI	Close to Ol6
Ol6	Fels	Ol, Opx, Mg-Hbl, Cr–Al-Spin	15	VI	2′778′707 1′129′665
Ol4	Fels/Vein	Ol, Opx, Mg-Hbl, Cr–Al-Spin	5	VI	Close to Ol6
Ol35	Fels	Ol, Mg-Hbl, Cr–Al-Spin	2	VI	Close to Ol6

Atg (antigorite), Ol (olivine), Di (diopside), Chl (chlorite), Ti-cl (Ti-clinohumite), Mt (magnetite), Cr-Mt (Cr-magnetite), Tc (talc), Trm (tremolite), Anth (anthophyllite), Opx (orthopyroxene), Mg-Hbl (Mg-hornblende), Cr-Al-spin (Cr-Al-spinel)

All hand specimens and thin sections are stored at the University of Bern, Switzerland. Swiss coordinates CH1903 +/LV95

talc-in rocks consist of characteristic acicular olivines that attain several centimetres in length (Fig. 4a). These olivines are embedded in a white, soft talc groundmass where antigorite is locally preserved in patches (Fig. 4a). Also, olivine-talc veins occur in zone **I&II** rocks consisting of white talc patches and elongated olivine grains (Fig. 4b). Microscopically, the talc-in paragenesis consists of unreacted antigorite serpentinite patches and its breakdown products, olivine, talc and chlorite (Fig. 4c and d). Both the antigorite-rich and olivine-talc-rich zones contain variable amounts of relic Cr-magnetite and magnetite (Sample 1603). At complete antigorite breakdown, two texturally distinct rock types occur, a massive granoblastic fels (Fig. 4e) and a pseudo-spinifex textured variety (Fig. 4f) which is only present in tremolite-poor rocks. Regarding the latter rock type, acicular olivines attain several tens of centimetres in length and are embedded in a talc-rich groundmass. Both rock types consist of the paragenesis olivine, talc and variable amounts of tremolite, chlorite and magnetite (Fig. 4g and h). Retrograde overprint is discernible where late serpentine replaces olivine along cracks (Additional file 3: Figure S2a).

4.1.3 Zone IV (200–70 m from the contact): anthophyllite + olivine

The mineral assemblage of zone **IV** is olivine, anthophyllite, chlorite, tremolite, Cr-magnetite, magnetite and serpentine (Fig. 5). The anthophyllite-in isograd is the most challenging to define in the field because steep topography and vegetation complicate outcrop access (Fig. 5a). At the outcrop scale, the olivine-anthophyllite dominated rocks form a massive fine grained fels (Fig. 5b). At the microscopic level, anthophyllite is acicular and forms a decussate texture with hypidioblastic olivine and chlorite and in lherzolitic bulk rocks additionally with tremolite. Together, these phases form the prograde paragenesis (Fig. 5c). Relic Cr-magnetite occurs in the olivine-anthophyllite-chlorite groundmass and both olivine and anthophyllite contain inclusions of magnetite. Zone **IV** is heavily retrogressed, where abundant pseudomorphic talc and antigorite replace anthophyllite, becoming indistinguishable from tremolites in the field (Fig. 5b and Additional file 3: Figure S2b). Additionally, olivine is often partially replaced by serpentine and magnetite.

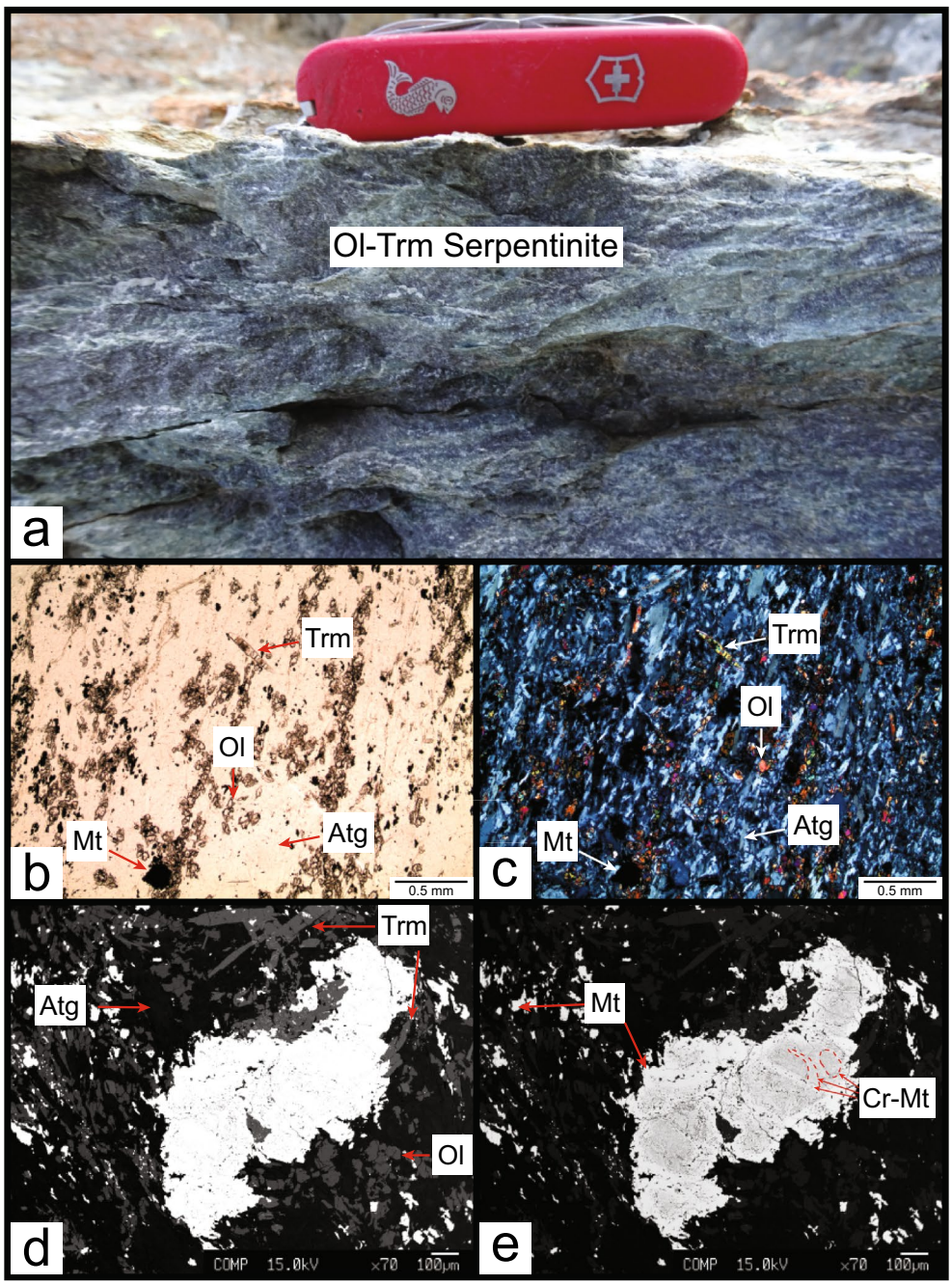

Fig. 3 **a** Zone **I&II** Antigorite-olivine-tremolite-serpentinite schist (Sample Ol21) (Swiss army knife 9 × 2.5 cm). **b** Plain polarised light image of antigorite-olivine-tremolite-serpentinite-schist containing large patches of antigorite, small sub-idioblastic olivine, acicular tremolite and minor sub-idioblastic magnetite. Olivine and antigorite form a mosaic texture. **c** Crossed polarised light image of **b**. Antigorite shows a preferred orientation with tremolite growing oblique to the foliation. **d** Backscatter image of acicular tremolite, sub-idioblastic olivine and dark antigorite. **e** Backscatter image of a large relic Cr-magnetite showing inclusion-rich darker cores and recrystallized magnetite-rich rims. Magnetite also occurs as groundmass grains

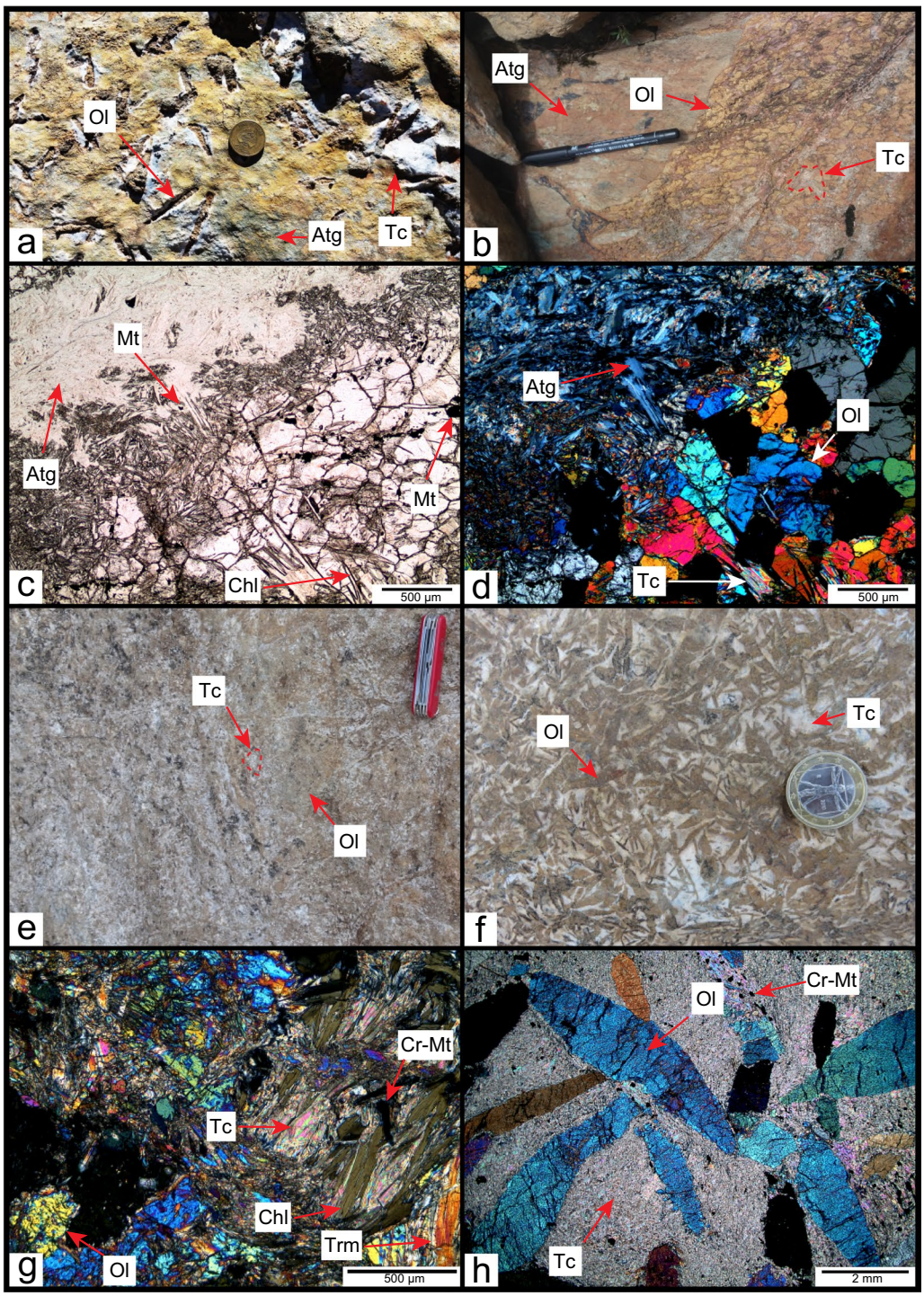

Fig. 4 Zone **III**: **a** Tc-in isograd locality above Alpe Zocca (Samples 1604, 1603) (coin diameter 2.3 cm). Large acicular olivine embedded in white talc and antigorite groundmass. **b** Olivine-talc vein at the talc-in isograd (Alpe Zocca, scale length 14.5 cm). **c** Plain polarised light image of the talc-in paragenesis (Sample 1603) with an upper antigorite-rich part and a lower part consisting of mosaic textured olivine-chlorite-magnetite. **d** Crossed polarised light image of **c**. Antigorite and fine grained interstitial olivine-talc in the upper part and mosaic textured olivine with talc next to chlorite in the lower part. **e** Massive granular olivine-talc fels (Sample Ol20, Swiss army knife 9 × 2.5 cm). **f** Pseudo-spinifex textured olivine-talc rock containing acicular olivine grains embedded in a white talc groundmass (Sample Ol16, Euro coin 2.3 cm in diameter). **g** Crossed polarised light image of granular olivine-talc fels containing chlorite, tremolite and Cr-magnetite (Ol20). **h** Crossed polarised light image of a pseudo-spinifex textured olivine-talc rock containing acicular olivine, fine grained talc and Cr-magnetite (Sample Ol16)

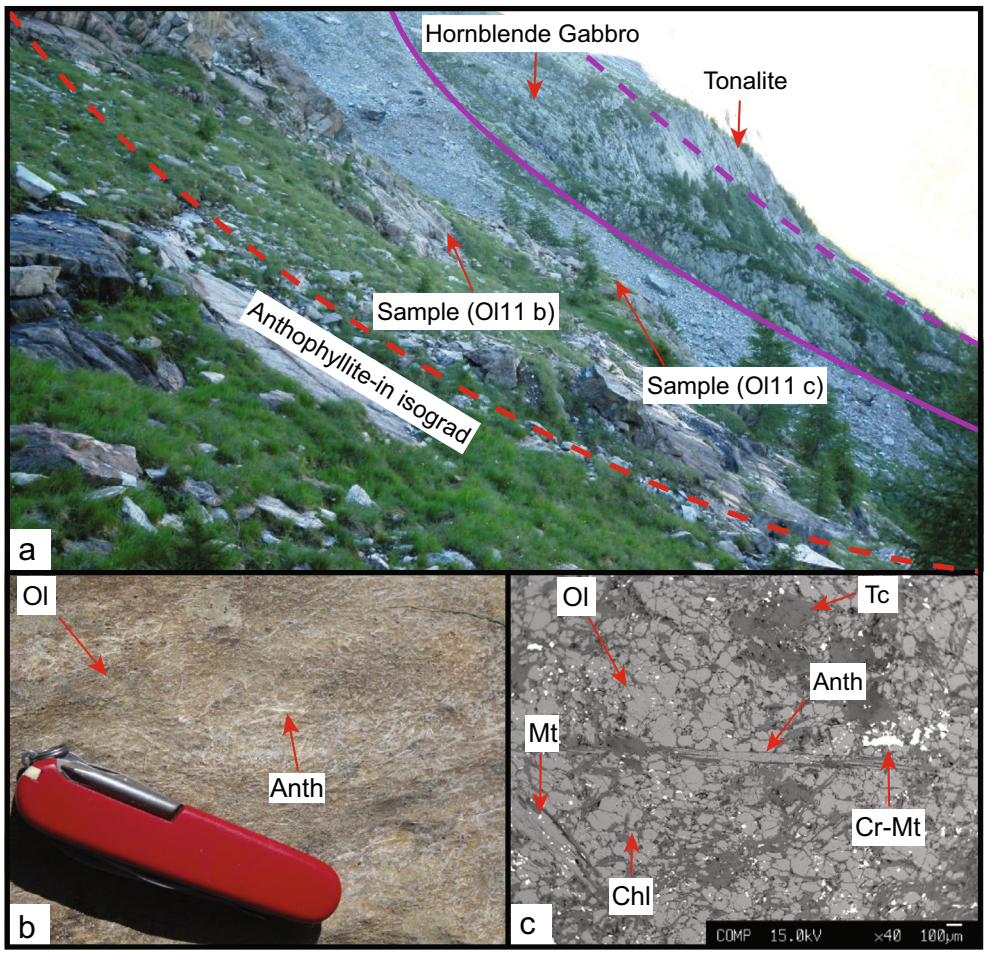

Fig. 5 Zone **IV**: **a** Photograph of the anthophyllite-in isograd (Val Sissone). In the background sample Ol11c and b locations and hornblende gabbro-tonalite borders are indicated. **b** Photograph of olivine-anthophyllite rock (Ol11c). **c** Backscatter image of sample Ol11c showing polygonal olivine with acicular anthophyllite, chlorite, talc and Cr-rich magnetite

4.1.4 Zone V (70 m from the contact): orthopyroxene-Mg-hornblende-(Cr–Al-spinel) appearance

The mineral assemblage of zone **V** is olivine, orthopyroxene, Mg-hornblende, tremolite, chlorite, Cr-Al spinel, anthophyllite, magnetite, talc and serpentine (Fig. 6). At the outcrop scale, the meta-serpentinites show a granoblastic texture consisting of brown olivine, orthopyroxene, white Ca-amphibole patches (Fig. 6a) and dark Cr–Al-spinel grains which are surrounded by light grey chlorite (Fig. 6b). At the microscopic scale, orthopyroxene is often intergrown with Ca-amphibole, which consists of three different zones (Fig. 6c). A tremolite-rich core (dark in BSE) which is rimmed by Mg-hornblende (bright in BSE) and small rims of tremolite (Fig. 6d). Orthopyroxene also contains inclusions of

(See figure on next page.)

Fig. 6 Zone **V**: **a** Photograph of the outcrop from zone **V** (Val Sissone), olivine-chlorite-orthopyroxene-(Al-spinel)-Mg-hornblende-anthophyllite rock with indicated white amphibole-rich patches and large single crystal olivine. **b** Photograph of a saw cut showing dark Al-spinel encircled by a greyish chlorite rim, grey orthopyroxene and brown olivine (tweezers 4.5 cm length). **c** Crossed polarised light image of sample Ol9 in zone **V** containing inclusion-rich orthopyroxene with Ca-amphibole intergrowth. **d** Backscatter image of **c** showing orthopyroxene containing inclusions of chlorite, olivine and a zoned Ca-amphibole intergrowth that consists of tremolite in the core, Mg-hornblende forming rim1 and tremolite rim2. **e** Backscatter image of orthopyroxene from sample Ol38 containing chlorite and olivine inclusions. **f** Backscatter image of sample Ol38 shows orthopyroxene intergrowth with anthophyllite. **g** Backscatter image of sample Ol38 exhibiting orthopyroxene with Al-spinel and chlorite inclusions. **h** Backscatter image of sample Ol38 containing a Cr–Al-spinel grain aggregate with sub-grains consisting of bright cores and darker rims. Retrograde replacement rims of Cr–Al-spinel consist of bright magnetite and dark chlorite

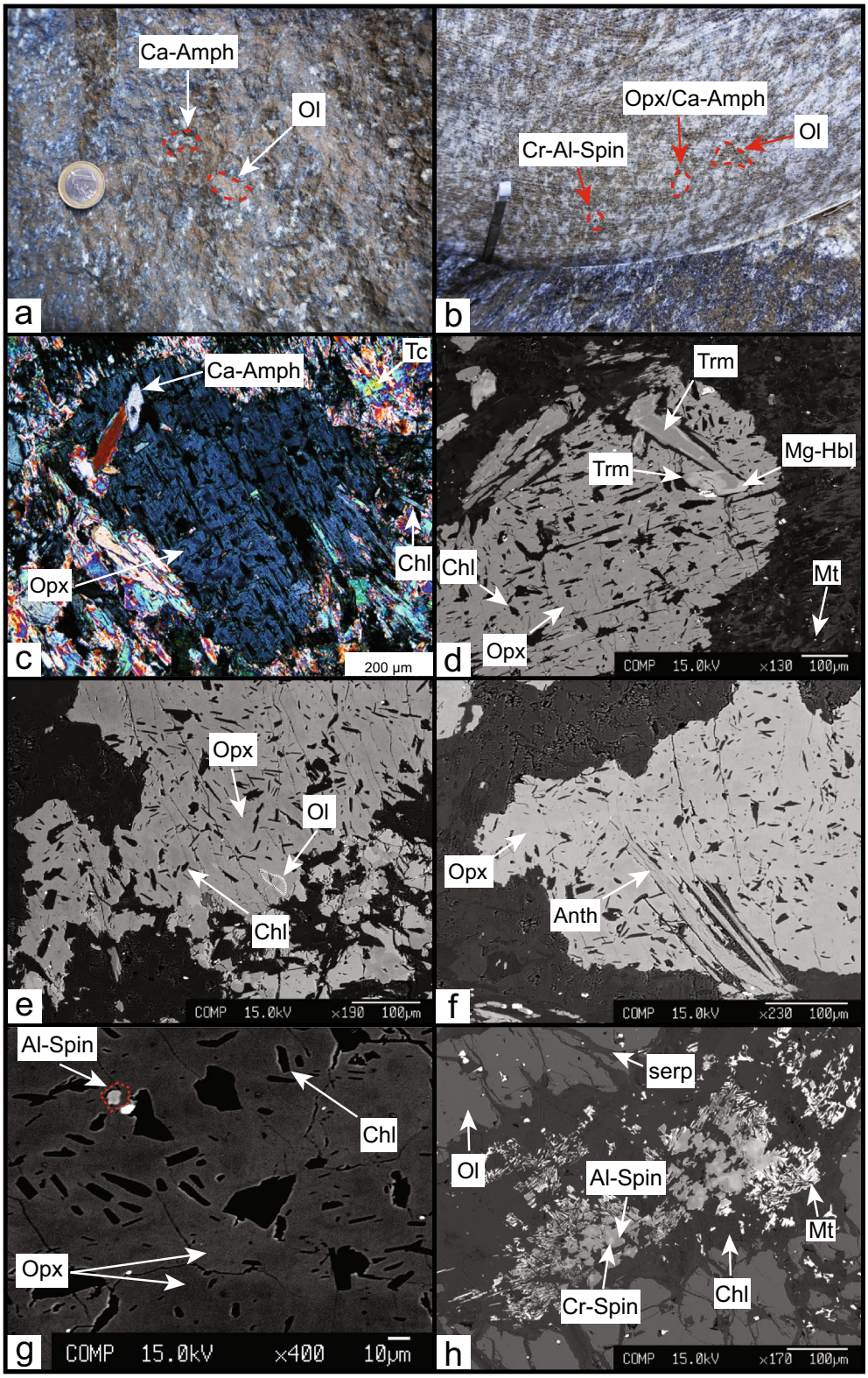

Fig. 6 (See legend on previous page.)

chlorite (Fig. 6d), olivine (Fig. 6e), anthophyllite (Fig. 6f) and a few micron sized Cr–Al-spinels (Fig. 6g). Moreover, orthopyroxenes are chemically zoned, visible as darker and brighter shaded zones in backscatter mode (Fig. 6g). Rare groundmass Cr–Al-spinels are concentrically zoned, showing decreasing reflectance towards their rims in backscatter mode (Fig. 6h). The association of Cr–Al-spinel, Mg-hornblende, orthopyroxene, anthophyllite, chlorite and olivine represents the peak metamorphic paragenesis of zone **V**. Retrograde overprint in zone **V** samples is manifested by the partial replacement of orthopyroxene by talc and Mg-hornblende by tremolite (Fig. 6c–d). Prograde Cr-Al-spinel is replaced at the rim by chlorite and magnetite and olivine is crosscut by late serpentine and magnetite (Fig. 6h).

4.1.5 Zone VI (40–0 m from the contact): chlorite and anthophyllite-out

The mineral assemblage of zone **VI** is olivine, orthopyroxene, Mg-hornblende, tremolite, Cr–Al spinel, chlorite, anthophyllite, magnetite and serpentine (Fig. 7). In zone **VI** metamorphic serpentinites form a triangular contact with the intrusion and metamorphosed gneisses of the Margna nappe (Fig. 7a). However, intrusive or metasomatic features such as veins, dykes, or blackwalls in the meta-serpentinites are absent. At the outcrop scale, the meta-serpentinites show a granoblastic texture (Fig. 7b). The most prominent field marker in the contact zone is black Cr–Al-spinel (Fig. 7b) often rimmed by chlorite (Fig. 7c) and large grey orthopyroxene, showing characteristic cleavage angles of 90° (Fig. 7b). Microscopically, most Cr–Al-spinels consist of multiple sub-grain aggregates (Fig. 7d and e). The subgrains show concentric zoning consisting of opaque to brown cores and brown to green rims (Fig. 7d) equivalent to decreasing reflectance in backscatter mode (Fig. 7e). Orthopyroxene and Mg-hornblende are occasionally intergrown (Fig. 7f) but mostly occur separately, forming the groundmass with olivine and Cr–Al-spinel (Fig. 7g). On one occasion, orthopyroxene is intergrown with olivine (Sample Ol6, Additional file 4: Figure S3a and b). The association of Cr–Al-spinel, Mg-hornblende, orthopyroxene and olivine represents the peak metamorphic paragenesis of zone **VI**. Retrograde overprint in zone **VI** is most prominently manifested by the formation of chlorite-magnetite replacement rims around Cr–Al-spinel (Fig. 7d, e and g). Also, anthophyllite either occurs as overgrowth rims around Mg-hornblende or as separate grains in the groundmass together with chlorite (Fig. 7g). Retrograded Mg-hornblende is often dissected by tremolite or shows tremolite rims (see Fig. 7g lower right corner), and olivine is replaced by late serpentine and magnetite.

4.2 Mineral compositions

Mineral compositions are described following increasing metamorphic grade. Analyses were acquired between direct grain neighbours. Mineral compositions are given in wt% oxides, element per formula unit (pfu) and molar ratios such as Mg# $[Mg/(Mg+Fe+Ni+Mn)] \times 100$ and yCr $[Cr/(Cr+Al+Fe^{3+})] \times 100$ in text. For most minerals, the compositional data set was recalculated assuming $Fe_{tot} = FeO$. Ferric iron contents were only recalculated for Cr–Al-spinel, Cr-magnetite and magnetite. The full data set is presented in Additional files 5, 6, 7, 8, 9, 10 and 11: Tables S1–7.

4.2.1 Olivine

Olivine from the regional metamorphic zone **O** shows homogenous low Mg# 86 in country rock sample Mal1101 and Mg# 90 in olivine veins (Samples Ol22 and Ol44). In contrast, zone **I&II** olivine (Sample Ol21) consists of homogeneously high Mg# 94. Zone **III** olivine displays the largest variability within a single metamorphic zone. At talc-in, olivine from an olivine-talc vein (Sample 1604) is richer in iron (Mg# 90) relative to the country rock sample 1603 (Mg# 91–92). Additionally, the latter olivines occasionally preserve Mg-rich cores (Mg# 92–93). At full antigorite breakdown, olivine from sample Ol20 shows homogeneous Mg# 88 and in sample Ol18 Mg# 90–91. In contrast, olivine cores from pseudospinifex textured sample Ol16 show slightly lower Mg#s than their rims with some intergrain variability, e.g., Mg# 86_{core}-88_{rim} or 87_{core}-89_{rim}. Olivine from zone **IV** exhibit homogeneous compositions of Mg# 90 (Sample Ol11c)

(See figure on next page.)

Fig. 7 Zone **VI**: **a** Contact between hornblende-gabbro, meta-gneisses and olivine-orthopyroxene-(Mg-hornblende)-(Cr-Al-spinel) rock (Samples Ol4, Ol6, Ol8 and Ol35) zone **VI**. **b** Photograph of the olivine-orthopyroxene-(Mg-hornblende)-(Cr-Al-spinel) rock containing large orthopyroxene grains with visible cleavage, brown-weathered olivine and black Cr–Al-spinel. **c** Photograph of elongated olivine, orthopyroxene and black Cr–Al-spinel encircled by greyish chlorite. **d** Plain polarised light image of Cr–Al-spinel consisting of a sub-grain aggregates with black Al-magnetite-rich cores and brown to green rims. Its outer boundary consists of retrograde magnetite-chlorite replacement rims and olivine in the groundmass. **e** Backscatter image zoom-in of **d** consisting of zoned Cr–Al-spinel aggregates with bright cores becoming gradually darker toward the rims. Magnetite and chlorite rims form the outer boundaries of the sub-grain aggregate. **f** Crossed polarised light image of inclusion-free orthopyroxene intergrown with Mg-hornblende. **g** Backscatter image of sample Ol6 showing the prograde paragenesis Cr–Al-spinel, Mg-hornblende, orthopyroxene and olivine. The retrograde assemblage consists of chlorite, anthophyllite, tremolite and late serpentine

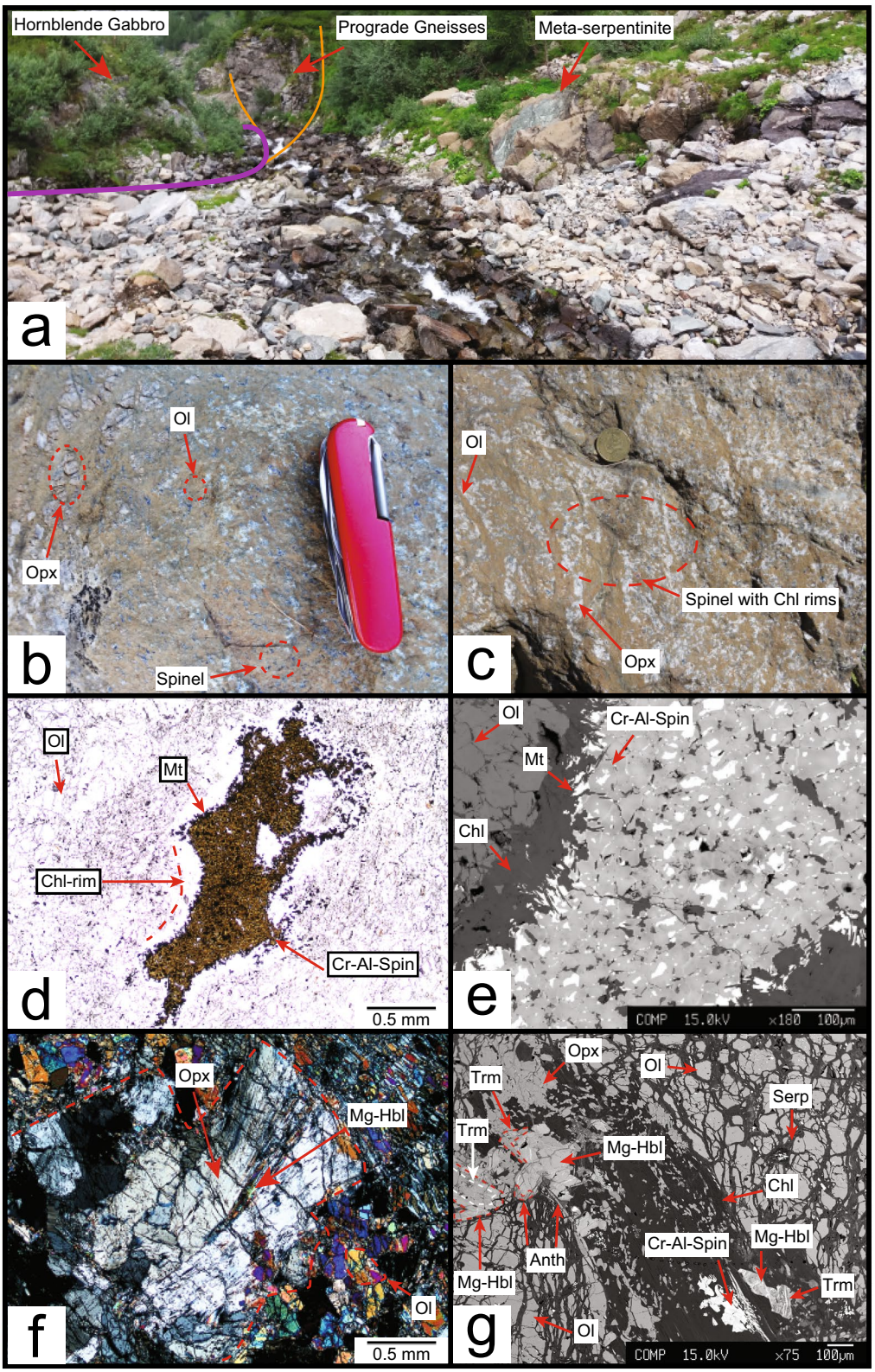

Fig. 7 (See legend on previous page.)

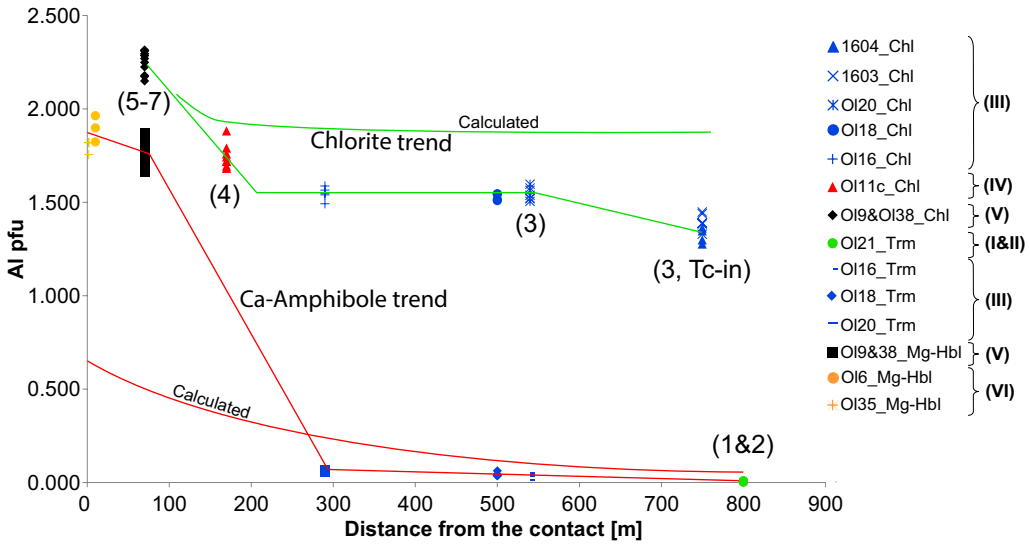

Fig. 8 Al pfu in Ca-amphiboles and chlorite shows a positive correlation with increasing metamorphic grade **I**–**VI** and decreasing distance from the contact. There are two distinct Ca-amphibole populations. One comprises zones **I**–**III** which represent tremolite stability, while the other comprises zones **V** and **VI**, representing Mg-hornblende stability. Chlorite shows four different populations, indicated by the green trend line. Two populations occur within zone **III** and one each in zones **IV** and **V**. For both chlorite and Ca-amphibole, calculated Al compositions from phase diagram section computation are also shown. Numbers in brackets correspond to the reactions presented in 5.1.1

whereas zone **V** olivine shows minor zoning (Mg# 87–88 in samples Ol9 and Ol38). Zone **VI** olivine of the contact paragenesis exhibits homogeneous Mg#s (89–90) only slightly varying between different samples (Ol6, Ol4, Ol35).

4.2.2 Ca-amphiboles (tremolite-Mg-hornblende)

Aluminium compositions of Ca-amphiboles show two separate populations following increasing metamorphic grade (Fig. 8). At its first appearance in zone **I&II** tremolite accommodates little Al. It is often below detection and at most contains 0.008 pfu, increasing to 0.060 Al pfu towards the end of zone **III** (Fig. 8). Al contents are significantly higher in zone **V** (1.66–1.87 pfu) and in zone **VI** (1.75–1.96 pfu), delineating the transition from tremolite to Mg-hornblende. Cr contents follow the same pattern with low contents of 0.002–0.023 pfu in zones **I**–**III** increasing to 0.03–0.09 pfu in zone **V** and 0.07–0.15 pfu in zone **VI**. Ti is below or above detection attaining maxima of 0.011 pfu in zone **I**–**III** tremolites but is significantly higher in zone **V**–**VI** Mg-hornblendes (0.08–0.11 pfu). Na contents are low but increase from 0.07 to 0.08 pfu through zones **I**–**III** while K is below detection. This changes abruptly in zone **V** where Mg-hornblende incorporates 0.35–0.53 Na pfu and 0.01–0.03 K pfu. In zone **VI**, Na contents are even slightly higher (0.45–0.54 pfu) while K is mostly lower (0.01–0.02 pfu) compared with zone **V** samples. Mg#s of tremolite generally decrease from 96–97 in zone **I&II** to Mg# 94–95 in zone **III** (Samples Ol20 and Ol16). The only exception is sample Ol18 showing similar Mg#s 96–97 as zone **I&II** tremolite. In contrast, Mg#s of Mg-hornblende (Mg# 86–89) in zones **V** and **VI** (Mg# 88–89) are lower than that of tremolite from zones **I**–**IV**.

4.2.3 Chlorite

Aluminium compositions of chlorite allow to distinguish four separate populations showing increasing Al content with decreasing distance from the intrusive contact (Fig. 8). At talc-in in zone **III**, the Al content in chlorite is lower (1.4–1.5 pfu) compared with zone **III** chlorite where antigorite breakdown was complete (1.6–1.7 pfu). Zone **IV** chlorite shows elevated Al contents (1.7–1.9 Al pfu) which is only exceeded by grains in zone **V** (2.2–2.3 Al pfu). At talc-in in zone **III** Cr compositions show the strongest variability of all samples, with very low to high contents (0.07–0.21 pfu). At full antigorite breakdown, Cr compositions are more homogeneous (0.09–0.18 pfu). This trend continues in zone **IV** grains showing Cr contents of 0.11–0.17 pfu. Close to its breakdown in zone **V**, both the compositional variability and absolute contents are low (0.03–0.09 pfu). Chlorite Mg# is fairly homogeneous throughout zones **III**–**IV**, varying between 93 and 94. Only one talc-in sample (1603) shows slightly elevated values (Mg# 94–95). In zone **V**, chlorite Mg#s are slightly lower, varying between 92 and 93.

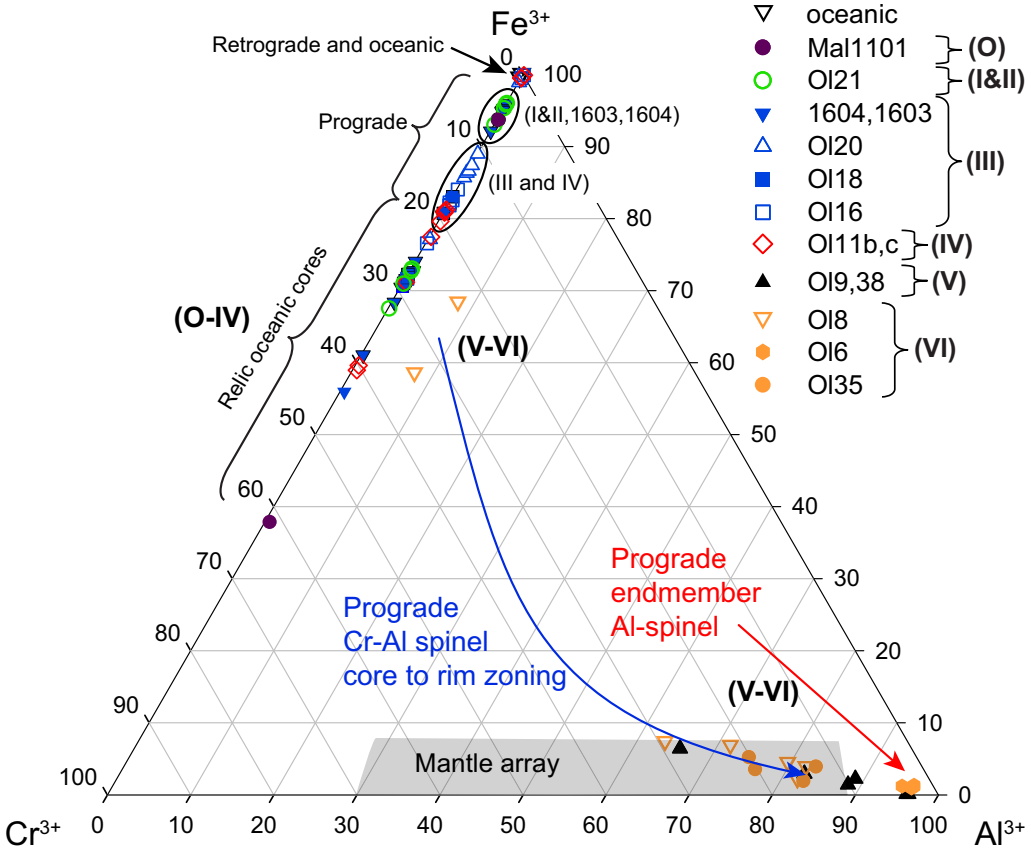

Fig. 9 Fe^{3+}–Cr^{3+}–Al^{3+}-Ternary diagram of magnetite, Cr-magnetite and Cr–Al-spinel (Additional files 5, 6, 7, 8, 9, 10, 11: Tables S1–7) from zones **O**–**VI**. The spinel type minerals show four main populations: low grade oceanic (Vils et al. 2008) and retrograde magnetite (Ol20, Ol16, Ol11b and c), relic oceanic Cr-magnetite cores, prograde Cr-enriched magnetite and prograde Cr–Al-spinel. The blue arrow indicates prograde core to rim compositions of Cr–Al-spinel from chlorite breakdown and the red arrow shows end-member compositions of Al-spinel inclusions in orthopyroxene of zone **V** (samples Ol9, Ol38) and groundmass grains in sample Ol6, zone **VI**. Low grade oceanic magnetite compositions are shown by the black "nabla" symbols. Additionally, the mantle compositional array modified from Kempf et al. (2020) is represented by the grey shaded area

4.2.4 Spinel group minerals (Magnetite, Cr-Magnetite, Cr–Al-Spinel)

The spinel-group compositional trends are represented by the trivalent cations Fe^{3+}, Cr^{3+} and Al^{3+} (see yCr, yFe, yAl in Additional files 5, 6, 7, 8, 9, 10, 11: Tables S1–7). Three groups of spinel group minerals are distinguished. Cr-magnetite and magnetite both lie on the chromite-magnetite join, showing Al contents close to the detection limit (Fig. 9). Large relic Cr-magnetite cores are characteristic of zones **I**–**IV**, showing high yCr (0.23–0.62) values (Fig. 9), while their inclusion-free rims have lower yCr numbers (0.06–0.16). The Cr content of groundmass magnetites and inclusions in olivine is low (yCr 0.04–0.05) from zone **I&II** (Sample Ol21) to talc-in in zone **III** (Sample 1604). These magnetites clearly form a separate population showing elevated yCr (0.16–0.19) at full antigorite breakdown in zone **III**, while the highest numbers are attained in zone **IV** (0.20). In contrast, post-peak retrograde magnetite is depleted in Cr and forms nearly pure end-member magnetite (Fig. 9). The third spinel group mineral is Cr-Al-spinel, which contains Al as a major element. Ferric iron decreases from core to rim and is mainly replaced with Al and to a lesser extent, Cr (Fig. 9). Zone **V** Cr–Al-spinel aggregates show yCr of 0.28 in cores, decreasing to 0.10 at rims. Additionally, nearly pure Al-spinel inclusions in orthopyroxene show yCr numbers as low as 0.04 (Fig. 9). Zone **VI** sub-grain aggregates show decreasing yCr from the core (0.34) to the rim (0.16). The lowest yCr number (0.02) was found in a large spinel aggregate in sample Ol6 (Fig. 7g).

4.2.5 Antigorite, talc, anthophyllite and orthopyroxene

Zone **O** antigorite (Sample Mal1101) accommodates 1.84–3.21 wt% Al_2O_3 and 0.06–1.36 wt% Cr_2O_3, and shows a homogenous Mg# 94. Antigorite in zone **I&II** is enriched in Mg (Mg# 96–97) and contains 0.43–2.68 wt% Al_2O_3 and 0.04–0.80 wt% Cr_2O_3. In both zones, Al_2O_3 and Cr_2O_3 contents positively correlate (Additional files 5 and 6: Tables S1 and S2). Talc contains minor amounts of Al_2O_3 (0.05–0.65 wt%) while Cr_2O_3 mass fractions can be below and above detection (b.d.-0.05 wt%). From talc-in throughout zone **III**, talc is Mg-rich showing Mg#s between 97 and 98 in samples 1604, 1603, Ol20 and Ol16 (Additional files 7 and 8: Tables S3–4). Anthophyllite is the most iron-rich silicate in the contact metamorphic serpentinites, with Mg#s between 86 and 88 in zone **IV** and Mg# of 85 in zone **V** (Additional files 9, 10: Tables S5 and S6). It also contains minor amounts of Na_2O in zone **IV** (0.01 and 0.09 wt%) and in zone **V** (0.03 and 0.06 wt%). All orthopyroxenes show characteristic lamellar growth zoning (Fig. 6g), accommodating 1.05 wt% to 1.56 wt% Al_2O_3 in dark and bright lamellae respectively (Sample Ol9) and 1.40–2.19 wt% in sample Ol38. The higher Al_2O_3 contents belong to the lighter shaded lamellae of the backscatter image. The Mg# in both samples ranges between 87 and 89. In zone **VI**, orthopyroxene intergrowths with olivine contain up to 4.35 wt% Al_2O_3, whereas lamellae in groundmass grains accommodate 1.06–2.98 wt% Al_2O_3 in sample Ol6 and 0.27–2.52 wt% in sample Ol4. They are slightly more Magnesian compared to zone **V** grains, showing Mg#s between 88 and 90.

5 Discussion

5.1 Reactions

Based on the observed mineral parageneses and various literature sources, we define prograde mineral reactions in the CaO–MgO–SiO_2–H_2O (CMSH) system for lherzolites and the MgO–SiO_2–H_2O (MSH) system for harzburgites. The participation of Al-rich phases in some reactions, e.g., antigorite, chlorite, Mg-hornblende and spinel group minerals, requires the addition of Al_2O_3 (Al) to the chemical system. Reactions involving TiO_2 (T) are cited from the literature. We explore compositional changes of minerals with respect to natural bulk rock compositions by considering the effects of FeO (F), Cr_2O_3 (Cr) and Fe_2O_3 (Fe^{3+}) and assume the presence of a H_2O-rich fluid.

5.1.1 Prograde reactions in the contact aureole

We derive the prograde reaction 1 from the paragenesis olivine + tremolite where diopside from the regional metamorphic zone reacted with antigorite (Evans & Trommsdorff 1970). Regarding the four observed phases and considering the free fluid as an additional phase, the reaction is univariant in CMSH.

$$\text{atg} + \text{di} = \text{trm} + \text{ol} + H_2O \quad (1)$$

This reaction is limited by the amount of diopside present in the serpentinites. In natural rocks, trivalent cations such as Al, Cr and Fe^{3+} can be accommodated as tschermak component in antigorite. If the tschermak component is saturated in antigorite, chlorite will additionally form (Padrón-Navarta et al. 2013). Tschermak saturation will particularly be attained in Al-rich (lherzolitic) bulks. Even though chlorite was not observed in sample Ol21, Trommsdorff and Evans (1972) have shown that chlorite may form through reaction 1. If chlorite is produced, some of the Cr and Fe^{3+} released by antigorite consumption may be incorporated into chlorite (Laird 1988) as well as in magnetite. Thus, the reaction would need to be described in the chemical system $CrFe^{3+}$CFMASH, in which it is no longer univariant:

$$\text{atg} + \text{di} = \text{trm} + \text{ol} \pm \text{chl} \pm \text{mt}_1 + H_2O \quad (1a)$$

Reaction 2 describes Ti-clinohumite breakdown to Mg-ilmenite and olivine (Trommsdorff & Evans 1980). It is univariant in the system MTH.

$$\text{Ti} - \text{cl} = \text{ol} + \text{ilm} + H_2O \quad (2)$$

This reaction is volumetrically unimportant in ultramafic rocks because even in fertile lherzolites, bulk TiO_2-contents are low (0.09–0.14 wt%, Müntener (1997)). Nevertheless, the coincidence with reaction 1 in the field from 1500 m to 750 m away from the contact (Fig. 2) allows defining the combined zone **I&II**. In the five component system CMSTH, the seven phase equilibrium is invariant.

The prominent talc-in isograd representing the onset of antigorite-breakdown is recognizable by the occurrence of white talc patches and elongated olivine. At complete antigorite breakdown, olivine and talc form the characteristic zone **III** paragenesis. Reaction 3 releases most of the water of all the reactions, and the consumption of Al-bearing antigorite leads to the formation of chlorite (Trommsdorff & Connolly 1996).

$$\text{atg} = \text{ol} + \text{tc} + \text{chl} + H_2O \quad (3)$$

While this reaction is univariant in MASH, the presence of ferrous iron renders the equilibrium divariant in FMASH. This is evident in the field, where talc and olivine occur in veins prior to the complete consumption of antigorite (Fig. 4a). According to Clément et al. (2019), the divariant zone is approximately 150 m wide in the field. The transition from partial to full antigorite

breakdown also indicates an enrichment of Cr in magnetite and, simultaneously, a decrease in ferric iron (Fig. 9). Large relic Cr-magnetites become sparse but their composition is more like that of magnetite in the groundmass and inclusions in olivine (Sample Ol16, Ol18 and Ol20, Fig. 9). Similar to reaction 1, ferric iron may be incorporated into newly formed chlorite. Thus, a reaction may be written considering the components $CrFe^{3+}FMASH$.

$$atg = ol + tc + chl + Cr - mt + H_2O \quad (3a)$$

The prograde formation of anthophyllite in reaction 4 is the first olivine-consuming reaction in the contact aureole. This reaction is univariant in MSH.

$$ol + tc = anth + H_2O \quad (4)$$

Relative to zone **III**, groundmass magnetite is enriched in Cr following the systematics outlined for reaction 3a (Sample ol11c, Fig. 9). Al contents are significantly increased in chlorite, forming a distinct chlorite population (Fig. 8). This can be expressed by the more complex reaction in the system, $CrFe^{3+}FMASH$.

$$ol + tc + chl_1 + mt = anth + Cr - mt + chl_2 + H_2O \quad (4a)$$

Orthopyroxene-bearing assemblages have been recognized in previous studies but have never been precisely documented (Bucher-Nurminen 1977; Riklin 1978; Trommsdorff & Connolly 1996; Trommsdorff & Evans 1972). The volumetrically most important orthopyroxene-forming reaction is the consumption of anthophyllite and olivine.

$$anth + ol = opx + H_2O \quad (5)$$

Reaction 5 is univariant in MSH but divariant in FMSH. This is in agreement with the observation of anthophyllite-orthopyroxene intergrowths (Fig. 6f).

Also, Bucher-Nurminen (1977) mentioned the presence of Mg-hornblende instead of tremolite in samples close to the intrusion contact but did not further investigate its occurrence. Robinson et al. (1982) suggested that in natural isochemically metamorphosed meta-serpentinites, this transition occurs simultaneously with the formation of spinel, which is supported by experimental investigations of Jenkins (1981, 1983, 1994).

$$trm + Cr - Al - spin = ol + Mg - hbl + H_2O \quad (6)$$

Indeed, the breakdown of chlorite to Cr–Al-spinel has not been described in the Bergell contact aureole yet. Chlorite inclusions in orthopyroxene that contain more Al than the clinochlore end-member (Fig. 8) are typical close to its breakdown (Jenkins & Chernosky 1986; Vavrecka-Sidler 1998). This is in agreement with nearly pure Al-spinel present as inclusions in orthopyroxene (Fig. 6g). Reaction 7 is univariant in MASH.

$$chl = ol + opx + Al - spin + H_2O \quad (7)$$

However, since Cr-magnetite is absent in parageneses **V** and **VI** and Cr–Al-spinel core compositions are aluminous, a Cr-magnetite-consuming reaction may be written.

$$chl + Cr - mt = ol + opx + Cr - Al - spin + H_2O \quad (7a)$$

In the chlorite and Cr-magnetite consuming reactions 7 and 7a, Cr and Fe^{3+} are released and partition into new phases such as Cr–Al-spinel, orthopyroxene and Mg-hornblende. The amount of calculated ferric iron in Cr–Al-spinel is very close to that of endmember Al-spinel with less than 5% magnetite. However, ferric iron estimates obtained by charge balance calculations depend on the normalization scheme applied and especially with regard to chlorite and Mg-hornblende, are inaccurate (Hawthorne et al. 2012; Laird 1988). Thus, ferric iron content and redox conditions, which are generally expected to become more reduced in rocks at increased temperatures (Frost 1991), cannot be resolved unambiguously.

All observations indicate that reactions 5–7 occurred simultaneously in the contact aureole. Hence, the six phase equilibrium of reactions 5 and 7 described in MASH is invariant, providing a tight constraint for pressure. In summary, all possible serpentinite dehydration reactions at low pressures occur in the Bergell aureole except Ca-amphibole dehydration where $Mg\text{-}hbl + ol = opx + plag + H_2O$ or $Mg\text{-}hbl + ol = opx + cpx + H_2O$.

5.1.2 Retrograde reactions and fluid flow

Post-peak retrograde overprint was chiefly controlled by H_2O-rich fluid infiltration because retrograde carbonates are absent. In zones **III**–**VI**, this is witnessed by the replacement of olivine with retrograde serpentine and end-member magnetite (Fig. 9). The more intense overprint in zone **IV** is additionally evidenced by serpentine, talc and magnetite pseudomorphs after anthophyllite (Fig. 9 and Additional file 3: Figure S2b).

$$anth + H_2O = tc + serp + mt \quad (8)$$

In zone **V**, the prograde phases orthopyroxene, Mg-hornblende and Cr–Al-spinel are replaced by talc, tremolite, chlorite and magnetite respectively (Fig. 6c and d). This is expressed by reaction 9.

$$\begin{aligned} &\text{opx} + \text{Mg} - \text{hbl} + \text{Cr} \\ &- \text{Al} - \text{spin} + \text{H}_2\text{O} \\ &= \text{chl} + \text{tc} + \text{trm} + \text{mt} \end{aligned} \quad (9)$$

Retrograde overprint in zone **VI** led to the partial replacement of Cr-Al-spinel with chlorite and magnetite (Fig. 7d and g). Mg-hornblende was replaced with tremolite and orthopyroxene with anthophyllite (Fig. 7g).

$$\begin{aligned} &\text{Mg} - \text{hbl} + \text{opx} + \text{Cr} - \text{Al} - \text{spin} + \text{H}_2\text{O} \\ &= \text{chl} + \text{anth} + \text{trm} + \text{mt} \end{aligned} \quad (10)$$

The fluid source causing the widespread retrograde overprint in zones **IV**–**VI** is poorly constrained. Thermal modelling has shown that hydrothermal fluid circulation cells may form around magmatic intrusions. They become active prior to magma emplacement and remain active during the cooling of the pluton, thus causing widespread retrograde overprint (Eldursi et al., 2009; Furlong et al., 1991). Therefore, several fluid sources may have continuously fed such a hydrothermal fluid circulation cell at the Bergell aureole. Internal fluids were released by prograde dehydration reactions in serpentinites and other lithologies parallel to the thermal front that has been moving away from the intrusion. External fluids were probably expelled by the tonalite intrusion where it became water saturated near its solidus (Reusser 1987).

5.2 Controls on the Al component in chlorite and Ca-amphiboles

The small increase of Al in chlorite from talc-in to fully equilibrated olivine-talc rock in zone **III** is explained by the presence of antigorite lamellae in chlorite. Because chlorite lamella in antigorite increase in abundance close to the breakdown of antigorite, a few antigorite lamella may have survived in what is now identified as chlorite (Shen et al. 2020; Wunder et al. 2001). Only minor amounts of Al are stored in prograde tremolite and talc. Thus, as soon as all antigorite lamellae break down, a constant Al composition of chlorite throughout zone **III** is attained. The increase of Al in zone **IV** chlorite may be explained by the addition of minor amounts from talc and is therefore assemblage controlled. In zone **V**, the Al composition of chlorite is buffered by Cr–Al spinel, which is in agreement with compositions reported from other studies dealing with samples close to intrusion contacts in meta-serpentinites (Frost 1975; Pinsent & Hirst 1977). The Al solubility in tremolite is buffered by the presence of antigorite in zone **I&II** and by chlorite in zone **III**. There is only a minute increase in Al changing from antigorite to chlorite buffering. This suggests that tremolite inclusions in Mg-hornblende in zones **V** and **VI** express Al buffering from chlorite of zone **IV**. Overgrowth rims of Al-rich Mg-hornblende on tremolite coincide with the presence of Cr–Al-spinel at chlorite breakdown. This coincidence has been observed in a number of studies on contact aureoles (e.g., Berg & Docka 1983; Bucher-Nurminen 1977; Frost 1975, 1976; Matthes & Knauer 1981; Pinsent & Hirst 1977; Robinson et al. 1982; Springer 1974). The Al composition of Mg-hornblende is also influenced by the bulk reactive alkali content, particularly by Na and K. The compositions reported here are typical for isochemically metamorphosed serpentinites at upper amphibolite facies conditions (Robinson et al. 1982). Even if fluid mobile elements like Na and K are depleted prior to contact metamorphism during oceanic serpentinization, where mantle clinopyroxene is replaced with diopside, some mantle clinopyroxene may have survived where diopside rims shielded them. This is visible in regional metamorphic zone **O** [Additional file 1: Figure S1 and Additional file 2, see also Müntener et al. (2010)]. Published bulk rock compositions from samples close to the magmatic intrusion show no evidence of fluid mobile element enrichment with Na_2O and $K_2O < 0.05$ wt% and no evidence for enrichment with SiO_2 or CaO (Trommsdorff & Evans 1972). Also, there is no direct field evidence for external fluid input from neighbouring sediments or the magmatic intrusion, i.e., no Ca-amphibole or phlogopite veins. The modal abundance of Mg-hornblende is very low in all samples (max 10 vol%), and we speculate that the minor Na content of the ultramafic bulk rock was concentrated in Mg-hornblende.

5.3 Fe–Mg partitioning between olivine and other phases

By measuring direct grain neighbours in thin section (Additional files 5, 6, 7, 8, 9, 10, 11: Tables S1–7), the order of preference for Fe relative to Mg between olivine and other phases is determined. It should be noted that the Mg# for all silicates is based on total iron as ferrous iron, i.e., $\text{Mg\#} = \text{Mg}/(\text{Mg} + \text{Ni} + \text{Mn} + \text{Fetot}) \times 100$. Only olivine rims were considered because cores may occasionally be inherited from a lower grade zone (Sample 1603, zone **III**) or show core to rim Mg-enrichment following increased temperatures during prograde growth (Sample Ol16, zone **III**). Figure 10 compiles all the data produced in this study and compares them with the best fits through compiled mineral pairs of corresponding parageneses from the literature (Additional file 12: Figure S4). The order of preference for Fe relative to Mg obtained from our data set is anthophyllite > orthopyroxene ≈ Mg-hornblende > olivine > chlorite > tremolite > talc.

The most reliable data for olivine-anthophyllite pairs is found in sample Ol11c **(IV)**, owing to minor

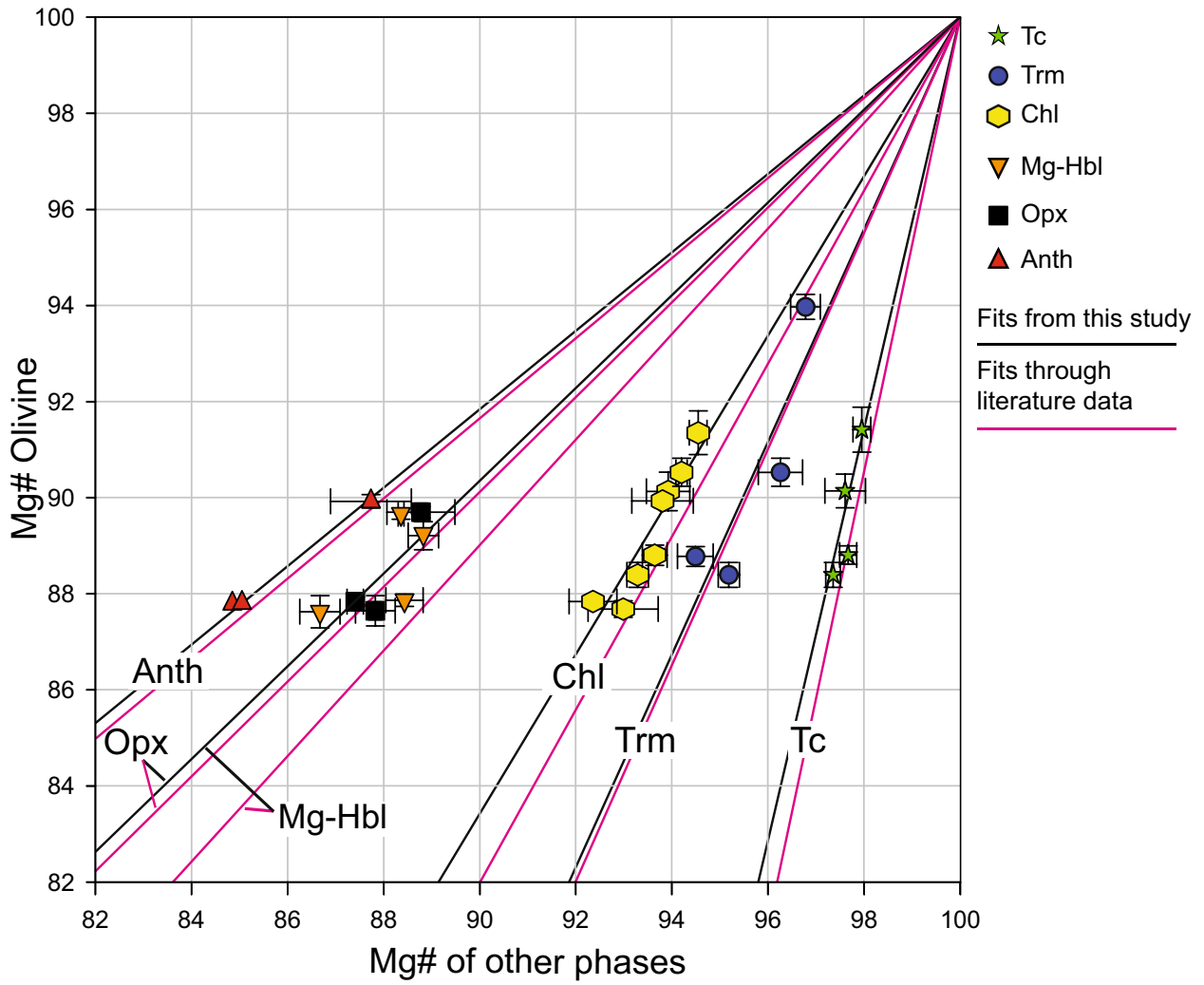

Fig. 10 Mg#s of olivine vs. paragenetic phases. Black fit lines per mineral are labelled in boxes representing partitioning trends. Pink lines show fits through complied mineral data pairs from the literature corresponding to the parageneses observed in this study (see discussion, Additional file 12: Figure S4)

retrogression and a well-equilibrated texture. The two points from samples Ol9 and Ol38 in zone **V**, however, represent single measurements because only one grain of anthophyllite is available per thin section. In contrast with Trommsdorff and Evans (1972), our data suggests that anthophyllite has lower Mg#s than equilibrium olivine (Fig. 10). This is in agreement with the fit through compiled mineral pair data from Springer (1974), Arai (1975), Frost (1975) and Matthes and Knauer (1981) (Additional file 12: Figure S4a).

Orthopyroxene from zone **V** samples Ol9 (single grain) and Ol38, as well as zone **VI** samples Ol4 and Ol6, show slightly lower Mg#s than olivine (Fig. 10). Even their lower Fe content lamellae, except for one measurement, show lower Mg#s than all olivine measurements (Additional file 11: Table S7). This is corroborated by the fit through compiled olivine-orthopyroxene pairs of Springer (1974), Arai (1975), Frost (1976), Berg (1977), Pinsent and Hirst (1977), Matthes and Knauer (1981), Berg and Docka (1983) and Nozaka (2011). Data of natural olivine-orthopyroxene pairs from Cerro del Almirez (Trommsdorff et al. 1998) and the experimental study of Padrón-Navarta et al. (2010) suggest 1:1 partitioning (Additional file 12: Figure S4b).

Mg-hornblende data from zones **V** and **VI** shows slightly lower Mg#s than olivine and similar partitioning to orthopyroxene. By contrast, the fit through compiled Mg-hornblende-olivine data pairs from Frost (1975), Frost (1976), Ashley et al. (1979), Matthes and Knauer (1981) and Springer (1974) suggests lower

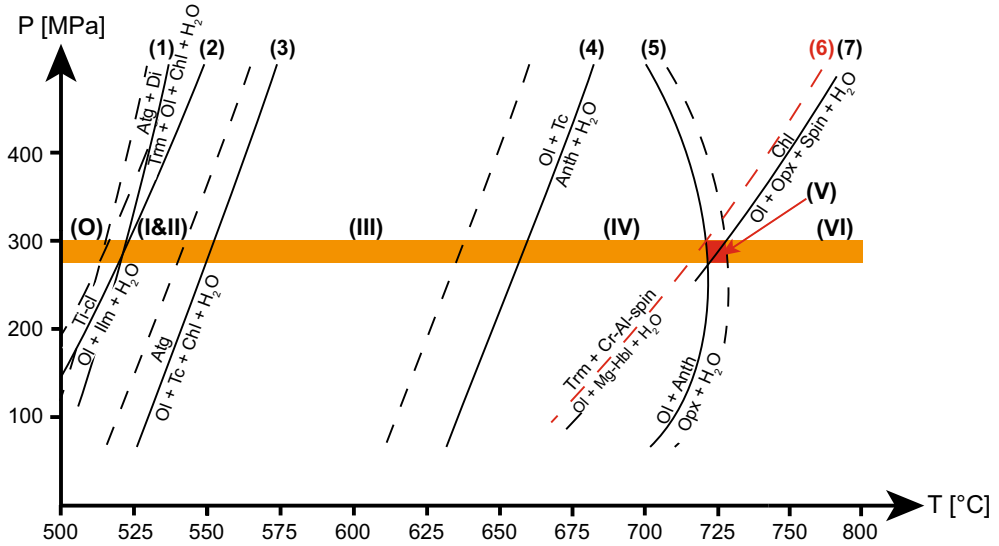

Fig. 11 Inferred phase relations are represented in a P–T diagram for lherzolitic serpentinites. Zones are indicated per reaction. Reaction 1 is from Evans and Trommsdorff (1970), reaction 2 from Trommsdorff and Evans (1980) and Weiss (1997), reaction 3 from Bowen and Tuttle (1949), Evans (1976) and Evans & Frost (1976), reactions 4 and 5 from Chernosky et al. (1985), Evans and Guggenheim (1988) and Nozaka (2011), reaction 6 is from this study and reaction 7 from Jenkins and Chernosky (1986). The orange bar indicates pressure estimates for contact aureole formation derived in the discussion

Mg#s for olivine, while individual studies have proposed controversial results (Additional file 12: Figure S4c). This is possibly caused by measuring intensely zoned grains. Zoning may be induced during prograde growth or partial retrograde equilibration. Additionally, Robinson et al. (1982) showed that Fe–Mg partitioning between Ca-amphibole-olivine pairs is dependent on the metamorphic grade. Accordingly, iron is progressively incorporated into Mg-hornblende from the upper amphibolite to the lower granulite facies.

Chlorite data from this study clearly shows higher Mg#s compared to olivine and coincides with the fit of Trommsdorff et al. (1998) (Fig. 10, Additional file 12; Figure 4Sd). The line through compiled olivine-chlorite pairs from Arai (1975), Frost (1975), Berg (1977), Pinsent and Hirst (1977), Matthes and Knauer (1981) and Berg and Docka (1983), and the one through experimental data of Padrón-Navarta et al. (2010) suggest even higher Mg#s for chlorite relative to equilibrium olivine. The fit provided by Matthes and Knauer (1981) contradicts all other approximations of the literature.

Tremolite Mg#s show a larger compositional range between different samples, which is similar to Mg-hornblende. The fits through our data and the compiled mineral pairs from the literature (Berg 1977; Berg & Docka 1983; Evans & Trommsdorff 1983; Frost 1975; Matthes & Knauer 1981; Nozaka 2011; Pinsent & Hirst 1977; Springer 1974) almost coincide and suggest higher Mg#s of tremolite relative to equilibrium olivine (Fig. 10). Lines provided by individual studies indicate even higher Mg#s in tremolite (Padrón-Navarta et al. 2010; Trommsdorff & Evans 1972; Trommsdorff et al. 1998). Only Springer (1974) reports lower Mg#s of tremolite with respect to our approximation (Additional file 12: Figure S4e).

Talc from zone **III** displays the most narrowly confined fit, closely approaching the line through compiled olivine-talc pairs of Berg (1977), Pinsent and Hirst (1977), Berg and Docka (1983), Nozaka (2011) and Trommsdorff and Evans (1972). By contrast, the approximation of Berg and Docka (1983) is nearly vertical, dissenting from any other published data (Fig. 10, Additional file 12: Figure S4f).

The overall excellent agreement between the observed Fe–Mg partitioning fits of this study and the one through selected mineral pairs of corresponding parageneses from the literature suggests that equilibrium compositions were measured. However, our approximations display a minor but systematic shift to the left in Fig. 10. This indicates that Fe partitioning relative to Mg in most silicates which are in equilibrium with olivine is stronger than previously thought. On the other hand, we argue that a shift to the right relative to our fits may be caused by using chemical analyses of retrogressed grains. For example, while olivine is stable over all prograde zones and only partially recrystallized at its rims, anthophyllite, orthopyroxene and Mg-hornblende are only stable in a narrow temperature field and hence more readily altered by retrograde fluids. Also, sheet silicates

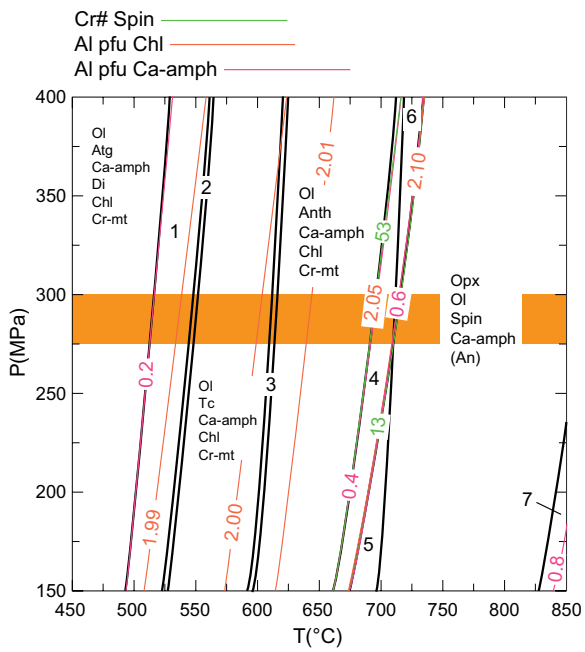

Fig. 12 P–T phase diagram section calculated with Perple_X. Coloured numbers and isopleths indicate Al pfu in chlorite, Ca-amphibole and Cr#s of spinel respectively. Calculated mineral parageneses are presented as mineral abbreviations (see text) in large divariant fields and as numbers in narrower fields. 1: Ol, Ca-amph, Chl, Cr-mt and Atg, 2: Ol, Ca-amph, Chl, Cr-mt, Atg and Tc 3: Ol, Tc, Anth, Ca-amph, Chl and Cr-mt 4: Ol, Spin, Anth, Ca-amph and Chl 5: Ol, Spin, Anth, Ca-amph and, (An) 6: Opx, Ol, Spin, Ca-amph and Chl 7: Opx, Ol, Spin, Ca-amph, Cpx and (An). (An) Indicates anorthite presence if not explicitly excluded from calculations. The orange bar shows pressure estimates for contact aureole formation derived from the discussion of Fig. 11

such as chlorite and talc are mechanically weaker, often finer grained, and have a higher surface-to-volume ratio than the other silicates, which makes them prone to retrograde Fe loss. Those arguments show why only analyses from samples with well-equilibrated textures and the least retrograde overprint should be used in order to establish Fe-Mg partitioning data. In particular, orthopyroxene, Ca-amphiboles and chlorite may also contain ferric iron, which would shift their Mg#s to higher values relative to olivine. However, following the discussion in Sect. 5.1.1, ferric iron content cannot be unambiguously determined for these phases.

Furthermore, prograde core to rim zoning of Mg#s in olivine also suggests that overstepping of the olivine forming reaction in zone **III**, as proposed by Lafay et al. (2019), was not significant and is generally not expected in serpentinites (Pattison et al. 2011).

5.4 Phase relations in serpentinites at low pressures

We derive phase relations by combining field observations and mineralogical data from this study with reaction curves from field and experimental studies from the literature (Fig. 11). According to Trommsdorff and Evans (1980), the univariant equilibria **1** and **2** have an invariant point at 300 MPa and 520 °C. This is consistent with Weiss's (1997) experimental brackets that indicate Ti-clinohumite breakdown at 300 MPa and 530 °C (Fig. 11). Divariant fields were estimated not to be broader than 10 °C (Trommsdorff & Connolly 1996; Trommsdorff & Evans 1972; Ulmer & Trommsdorff 1999). Therefore, pressure during contact metamorphism is well constrained at 300 ± 30 MPa. At the corresponding pressure, reaction 3 was placed according to the experimental brackets of Chernosky et al. (1985) at 550 °C. For a natural reactive bulk of Mg# 90 its position may be about 10 °C lower (Trommsdorff & Connolly 1996; Ulmer & Trommsdorff 1999), which is in excellent agreement with a 150 m wide zone where antigorite, olivine and talc coexist (Clément et al. 2019). Reaction 4 was placed at 650 °C according to the experimental brackets of Chernosky et al. (1985). This reaction shifts about 20 °C down temperature for a reactive bulk of Mg# 90 (Evans & Guggenheim 1988; Nozaka 2011; Trommsdorff & Connolly 1996; Ulmer & Trommsdorff 1999). Zone **V** paragenesis is particularly important due to the completion of reactions 5, 6 and 7. The intersection of reactions 5 and 7 is probably very close to the invariant point in MASH at 720 ± 10 °C and 275 ± 30 MPa (Jenkins & Chernosky 1986), with the difference that instead of cordierite, anthophyllite is involved in the equilibrium. Reaction 6 commences at the onset of reaction 7, and therefore the sharp transition from tremolite to Mg-hornblende occurs within the intersecting divariant fields of reactions 5 and 7. In P-T space, this divariant intersection field is likely not exceeding 10 °C (Evans & Guggenheim 1988; Trommsdorff & Connolly 1996; Ulmer & Trommsdorff 1999). The pressure of contact metamorphism in the meta-serpentinites is therefore constrained to ~ 300 MPa (orange rectangle in Fig. 11) by the invariant equilibria **1**–**2** at the outer and **5**–**7** at the inner part of the aureole.

5.5 Comparison with calculated phase diagram sections

Following the above discussion, a phase diagram section (Fig. 12) was calculated over a temperature range from 450 to 850 °C and pressures between 150 and 400 MPa. TiO_2 was not taken into account due to the lack of solution models for Ti-clinohumite. We have also excluded ferric iron from our calculations due to the lack of independent thermodynamic data for the key phases considered here. Overall, the sequence of calculated

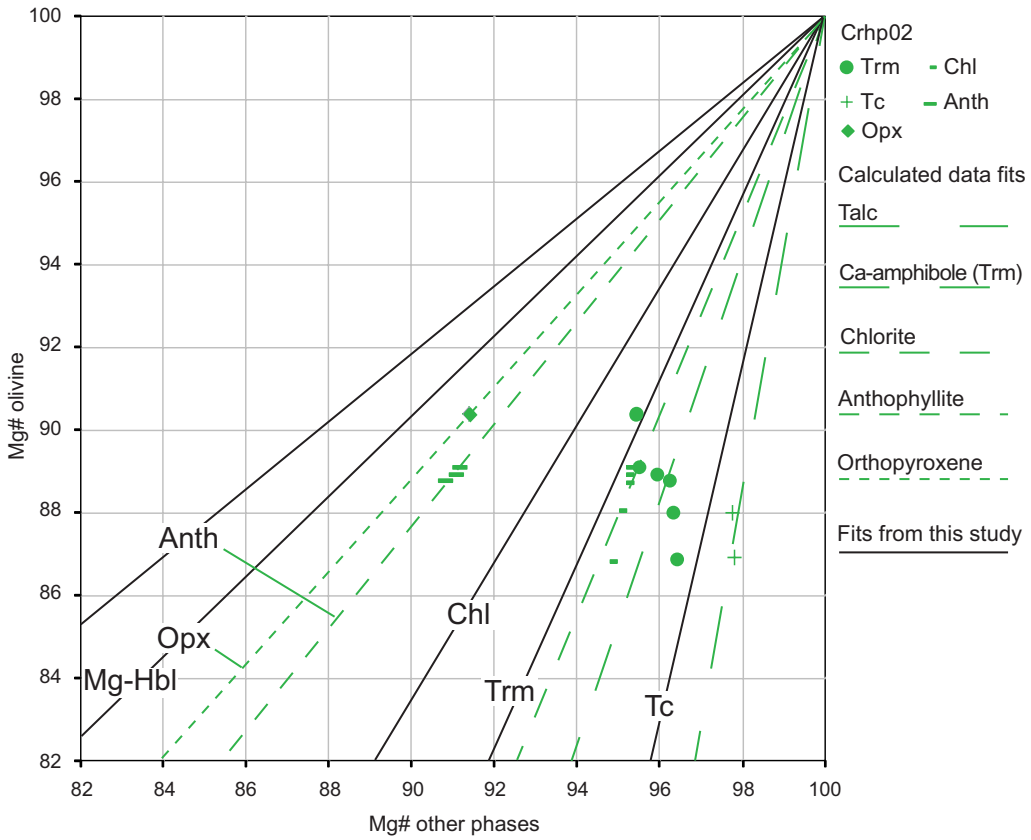

Fig. 13 Mg#s of olivine vs. paragenetic phases from phase diagram section computation (using the 2002 revised data base of Holland and Powell (1998) augmented with Cr (Klemme et al. 2009) and corresponding solution models) are represented by the dashed fits and compared with the fits from this study. Partitioning between olivine and other phases was calculated for temperatures listed in Additional file 13: Table S8: Opx (750 and 800 °C), Anth (650, 675, 700 °C), Chl (500, 550, 600, 650, 675 and 700 °C), Ca-amphibole (500, 550, 600, 650, 675, 700, 750 and 800 °C) and Tc (550 and 600 °C)

assemblages is consistent with the order of olivine-tremolite-chlorite, olivine-talc-chlorite, olivine-anthophyllite-chlorite, olivine-orthopyroxene-chlorite and olivine-orthopyroxene-spinel. The position of the intersection between anthophyllite-out and chlorite-out is also correctly predicted when using the 2002 revised Holland and Powell (1998) data base (Fig. 12 and Additional file 14: Figure S5). The discrepancy between the observed and the calculated parageneses is greater when using the latest Holland et al. (2018) database including corresponding solution models (Additional file 15: Figure S6). For example, orthopyroxene is predicted between 450 and 500 °C and the intersection of anthophyllite-out and chlorite-out is not reproduced. Additionally, two distinct orthopyroxenes are predicted above 750 °C. Following those arguments, the remainder of the discussion refers to results obtained with the 2002 data base. A major difference between the computed phase relations and those observed in natural rocks is the predicted co-occurrence of tremolite and diopside below 500 °C, which was not observed in this study, or by Trommsdorff and Evans (1972). After the classification of Leake et al. (1997), tremolite is predicted throughout the calculated P–T section. This is in agreement with the tremolite presence in zones **III** and **IV** and the compositions reported in this study as well as those in Trommsdorff and Evans (1972). Tremolite is also the sole Ca-amphibole phase predicted above 700 °C, whereas in natural rocks, Mg-hornblende is additionally present. Instead of Mg-hornblende, plagioclase is predicted in the computed phase diagram section above chlorite breakdown, which is not supported by our observations or other studies in similar geological settings (Frost 1975; Matthes & Knauer 1981; Pinsent & Hirst 1977; Springer 1974; Tracy & Frost 1991). Therefore, the sequence of natural parageneses can only be reproduced between 500 and 700 °C. Plagioclase has

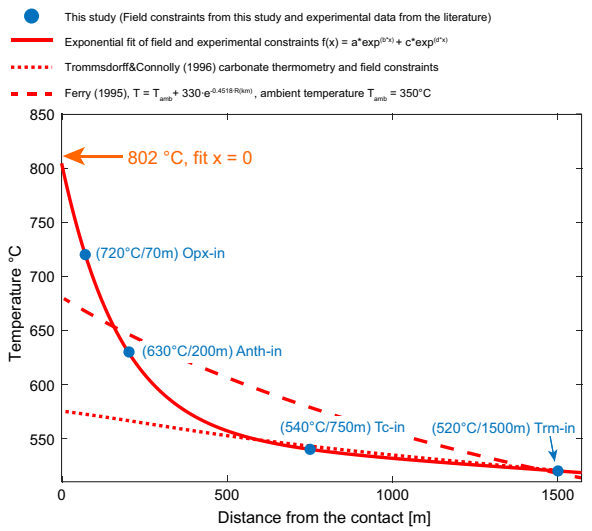

Fig. 14 MATLAB based temperature profile fit of the north-eastern transect through data points derived in Fig. 11. The two other temperature profiles for the Bergell contact aureole are from Ferry (1995) and Trommsdorff and Connolly (1996)

only been reported from two contact aureoles in contact zones between meta-serpentinites and mafic hornfels (Docka et al. 1986; Frost 1976). It is also absent in meta-serpentinite lenses from the Lepontine Alps that formed between 0.5–0.8 GPa and 700–800 °C (Stucki 2001; Trommsdorff 1974). Frost (1976) suggested that at pressures below 1 GPa and temperatures above 700 °C, the stable parageneses up-temperature are meta-(Mg-hornblende)-spinel peridotite, (Mg-hornblende)-plagioclase peridotite and then plagioclase peridotite. The increased stability of Mg-hornblende relative to tremolite and plagioclase is due to the incorporation of Al, Na, Ti and K (Robinson et al. 1982). Moreover, these elements have been shown to increase with temperature and pressure, stabilizing Ca-amphiboles to temperatures above 1000 °C and pressures up to 2.8 GPa (Mandler & Grove 2016; Niida & Green 1999).

In contrast to natural mineral pairs, the order preference for Fe relative to Mg extracted from phase diagram sections is: olivine > orthopyroxene > anthophyllite > chlorite > tremolite > talc (Fig. 13). The relative position of olivine and anthophyllite is inversed, but the remaining phases show the same order. In absolute numbers, however, olivine shows a higher preference for Fe relative to Mg and thus lower Mg#s than the other phases, shifting all fits to the right in Fig. 13 (see also Additional file 13: Table S8).

The calculated Al compositions for chlorite show only a minor change from 500 to 700 °C (1.99–2.1 Al pfu), remaining close to clinochlore composition (Fig. 8). In contrast, natural chlorites accommodate between 1.3 and 2.3 Al pfu. Thus, Al compositions in models are overestimated at low temperatures and underestimated close to chlorite breakdown. Both, calculated and natural spinel show decreasing Cr#s from core to rim. However, absolute numbers cannot be directly compared due to ferric iron presence in natural spinels.

5.6 Temperature profile through the Bergell aureole

The isograd temperatures and their distances from the contact derived from section 5.4 [Trm-in (1500 m, 520 °C), Tc-in (750 m, 540 °C), Anth-in (200 m, 630 °C) and Opx/Hbl-in + Chl-out (70 m, 720 °C)] were fit to the following equation:

$$T = a \cdot e^{(b \cdot x)} + c \cdot e^{(d \cdot x)} \quad (11)$$

With a = 249.3, b = − 0.00559, c = 553, d = − $4.113 \cdot 10^{-5}$ and x = distance from the contact in meters. By using this parametrization, the peak metamorphic temperature of each sample from zones **I**–**VI** can be estimated. The contact temperature between the Bergell intrusion and meta-serpentinites is then obtained by setting x = 0, returning a contact temperature of 802.3 °C. Further evidence for contact temperatures close to 800 °C is provided by the occurrence of orthopyroxene in meta-pelites at the contact in Val Predarossa (Wenk et al. 1974). Contact temperatures above 700 °C are also corroborated by the presence of wollastonite in silicic marbles (Bucher-Nurminen 1977), sillimanite in pelitic schists (Wenk et al. 1974), the anorthite content of plagioclase in mafic rocks (Riklin 1978), and brucite pseudomorphs after periclase in metamorphic dolomites (Trommsdorff & Schwander 1969). In any case, our new temperature estimate is 230 °C higher than the one of 570 °C from Trommsdorff and Connolly (1996), and all estimates from the other lithologies would also predict orthopyroxene stability in meta-serpentinites under H_2O saturated conditions. According to Trommsdorff and Connolly (1996), orthopyroxene would also become stable if the CO_2 activity in the fluid was high enough to destabilize hydrous phases such as anthophyllite. However, if this were the case, tremolite should have broken down to either plagioclase or clinopyroxene, which were both not observed in contact rocks. Therefore, the presence of Mg-hornblende in contact samples indicates that the fluid was H_2O-rich and released by the suggested breakdown reactions.

Ferry (1995) proposed a simple heat conduction model based on similar equations provided by Furlong et al. (1991). For an ambient temperature of 350 °C in the country rock, this model predicts a contact temperature of 680 °C, which is 120 °C lower than our estimate (Fig. 14). Even though this estimate is closer to the temperature required for orthopyroxene formation (Fig. 11),

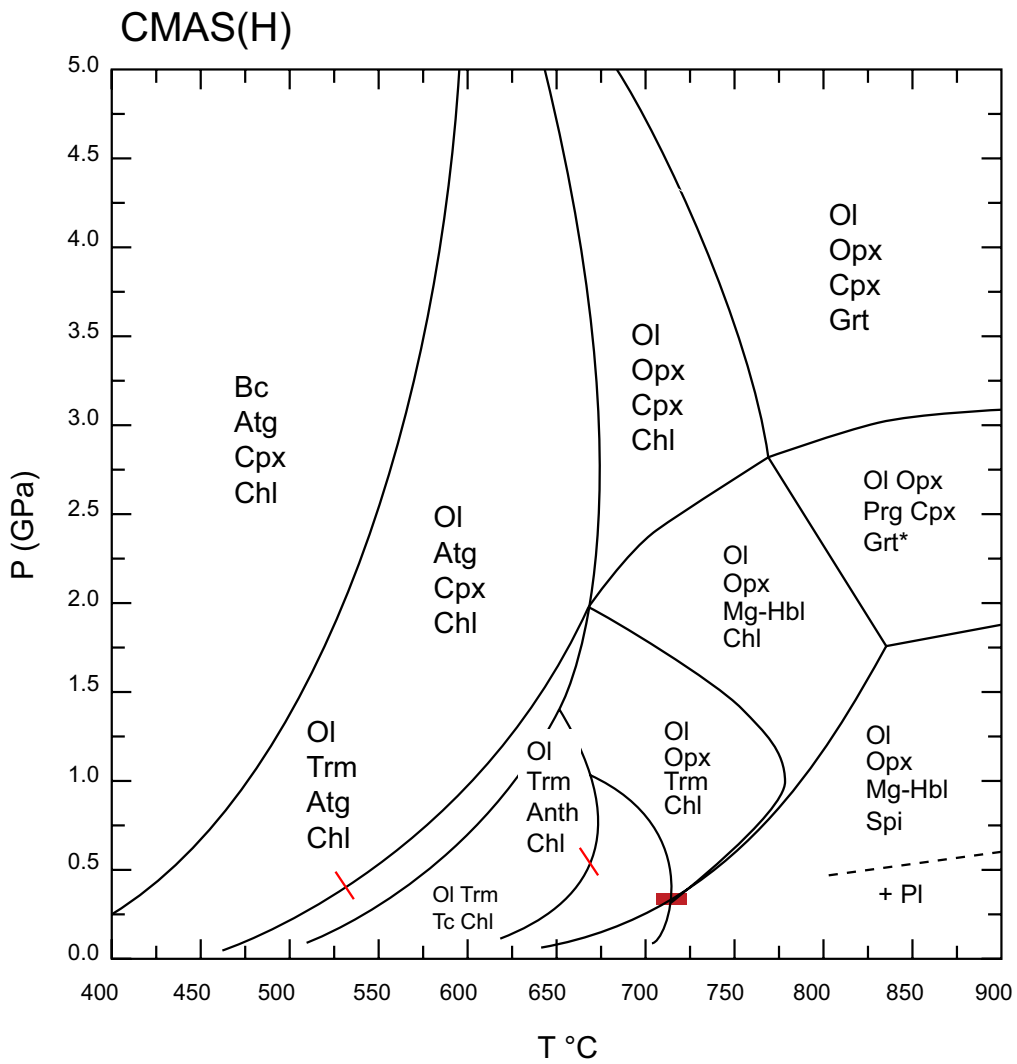

Fig. 15 Petrogenetic grid from 400 to 900 °C and 0.0–5.0 GPa using Figs. 11 and 12 for low pressure phase relations (0.1–0.4 GPa), data from Stucki (2001), Frost (1976) and Niida and Green (1999) for medium pressures (0.4–1.0 GPa). Mysen and Boettcher (1975), Jenkins (1983), Niida and Green (1999) and Fumagalli and Poli (2005) for high pressures (1.0–5.0 GPa). The red bar shows the intersection of reactions 5–7, and plagioclase stability is indicated by the dashed line according to Jenkins (1983). *Note that either Mg-hornblende or chlorite may be the limiting phases for garnet (Grt), clinopyroxene and pargasite (Prg) production depending on the chosen Ca and Al bulk, including Na in natural rocks

it would still be in the anthophyllite zone **(IV)**. It also predicts that the talc-in reaction occurs 1200 m from the contact, which is not supported by field evidence (Table 1, Fig. 2). In any case, the predicted temperature for zone **V** from this study is higher than both proposed contact temperatures from Ferry (1995) and Trommsdorff and Connolly (1996). Our observations suggest that post-peak metamorphic fluid infiltration led to partial or full replacement of orthopyroxene by anthophyllite or talc. Hence, the more intense retrogression, particularly in zones **V** and **VI**, may have led previous studies to conclude that locally CO_2-enriched fluids produced orthopyroxene and anthophyllite-orthopyroxene bearing assemblages at lower temperatures.

Since the adjacent hornblende-gabbro and tonalite show well crystallized equigranular textures, the intrusion was likely liquid at the time of emplacement. Reusser (1987) suggested that magma of ~ 900 °C intruded the surrounding country rocks, which had an ambient temperature of about 350 °C. Because of the high contact temperature of 800 °C and the shape of the temperature profile inferred here, alternative models to simple heat conduction must be considered. Jaeger (1961) argued that intrusion geometry is the most important factor that

controls temperatures around magmatic intrusions (see also Furlong et al. 1991 and references therein). This argument has been used by Riklin (1978) to explain the varying width of the contact aureole produced by the Bergell intrusion. More recently, Annen (2017) proposed that the relative thermal diffusivities between magma and country rock may have a significant impact on aureole widths. Also, multistage magma pulses may enlarge thermal aureoles. This model was also used by Floess and Baumgartner (2015) to explain the higher contact temperatures derived from meta-sediments at the Adamello batholith.

5.7 Implications for other geodynamic settings

5.7.1 Subduction zones

We have shown that chlorite composition in the computed phase diagram section is close to the clinochlore endmember (Fig. 8). However, natural chlorites from the contact aureole and subducted high-pressure serpentinites, e.g., Zermatt, Cerro del Almirez and Cima di Gagnone only contain 1.4–1.5 Al pfu and 1.5–1.6 Al pfu respectively, at equilibration temperatures between 550 and 750 °C (Kempf et al. 2020; Padrón-Navarta et al. 2010, 2011; Pfiffner 1998; Scambelluri et al. 2014; Trommsdorff et al., 1998). Chlorite only assumes higher Al contents than clinochlore at its breakdown at low and high pressures (Fumagalli & Poli 2005; Fumagalli et al. 2014; Jenkins & Chernosky 1986). By assuming a fixed bulk composition, the Al ratio between calculated clinochlore and natural pennine is 2.0/1.6 = 1.25 for Cima di Gagnone and the one for Cerro del Almirez is 2.0/1.5 = 1.33. Therefore, 25–33 mol% more chlorite must be present in natural rocks where chlorite is the only Al-bearing phase. Thus, when using standard thermodynamic data bases and corresponding solution models, the molar chlorite content in subducted serpentinites is underestimated except close to its breakdown. Furthermore, chlorite is stable to higher pressures and temperatures than antigorite (Fumagalli & Poli 2005; Fumagalli et al. 2014; Goto & Tatsumi 1990; Padrón-Navarta et al. 2013; Pawley 2003), so calculated phase diagram sections overestimate fluid release by antigorite breakdown and underestimate fluid production by chlorite breakdown.

Our field study showed that the transition from tremolite to Mg-hornblende in meta-serpentinites occurs simultaneously with the chlorite breakdown reaction, forming spinel. Also, Stucki (2001) has shown that the tremolite to Mg-hornblende transition occurs between 750 and 800 °C at pressures typical for barrovian metamorphism (0.5–0.8 GPa). Hence, up to about 1 GPa, the slope of the tremolite to Mg-hornblende transition follows the chlorite breakdown curve which is in agreement with Frost (1976). According to field and experimental studies, this transition did not occur in prograde Ca-amphibole from Cerro del Almirez, formed between 650–700 °C and 1.7–1.9 GPa where chlorite is the stable Al phase (Padrón-Navarta et al. 2010; Trommsdorff et al. 1998). However, at Cima di Gagnone, Mg-hornblende is in equilibrium with garnet in metamorphosed serpentinites that equilibrated between 750 and 800 °C at ~ 3 GPa (Evans & Trommsdorff 1978; Scambelluri et al. 2014). Jenkins (1983) determined the upper stability limit of tremolite coexisting with olivine and showed that the reaction has a backbend and is bracketed at 650 °C and 2 GPa. Fumagalli and Poli (2005) reported that Al-rich tremolite is stable at 700 °C up to 2.4 GPa in a hydrous lherzolite composition, but no Ca-amphibole at 750 °C and 3 GPa. This may suggest that the tschermakite component in Ca-amphibole increases with pressure, for which we tentatively propose a chlorite + Mg-hornblende (Al-tremolite) field in CMASH above 650 to 750 °C and 2.0 down to 1.0 GPa, respectively (Fig. 15). The stability limit of pargasitic amphibole containing Na as a major constituent was found to be just above 3 GPa at 925 °C (Niida and Green 1999). Ca-amphibole presence also influences the transition from Mg-hornblende-spinel and chlorite peridotite to garnet peridotite. According to the experiments of Mysen and Boettcher (1975), the Mg-hornblende-spinel peridotite reaction is placed at 1.75 GPa and 830 °C with a gentle positive slope. Between 1.8 and 2.8 GPa, the reaction of chlorite + Mg-hornblende ± orthopyroxene—> garnet + clinopyroxene + pargasite ± olivine + fluid marks the transition between the hornblende-chlorite peridotite and the pargasite-garnet peridotite fields. At pressures below 1.8 GPa and down to 1.0 GPa, Mg-hornblende-chlorite peridotite reacts to Mg-hornblende-spinel peridotite along the chlorite breakdown reaction. Plagioclase formation is likely to occur below 925 °C at 0.5 GPa (Niida & Green 1999), but above 850 °C (Jenkins 1983).

5.7.2 Subduction initiation and infancy

Figure 15 was constructed based on prograde dehydration reactions derived from natural samples and bracketed experiments for upper and lower crustal environments, including the lithospheric mantle. The established phase relations in hydrous ultramafic rocks at low-pressure conditions are not only relevant for contact metamorphism. Similar high geothermal gradients can occur during the formation of oceanic core complexes at slow-spreading ridges such as the Atlantis massif (Schroeder & John 2004), at transform faults (Prigent et al. 2020) or during subduction initiation of young oceanic lithosphere (Agard et al. 2020).

In oceanic transform faults, the Mg-hornblende-spinel-olivine-orthopyroxene paragenesis has been reported to occur at 20–25 km depth (see Fig. 8, Prigent et al. 2020). Serpentinization of deep mantle fractures and faults at intra-oceanic transitions has been proposed to create weak zones such that spontaneous subduction initiation may occur along them (Dymkova & Gerya 2013; Stern & Gerya 2018). At passive continental margins, variably hydrated mantle faults, shear zones, and mylonites (Vissers et al. 1995) show the same parageneses as the deep oceanic transform faults (Prigent et al. 2020) or oceanic core complexes (Schroeder & John 2004). Hydration reactions reduce the rheological strength of these faults such that negatively buoyant oceanic lithosphere may detach along them and initiate spontaneous subduction (Hilairet et al. 2007; Hirauchi et al. 2016; Karig 1982; Van der Lee et al. 2008). According to Regenauer-Lieb et al. (2001), the detachment process could be enhanced by topographic loading of sediments.

Regarding spontaneous subduction initiation, we propose that by sinking of the negatively buoyant oceanic lithosphere into deeper levels, hydrated mantle faults will experience prograde metamorphism. Dehydration reactions along the sinking weak zones would decrease the rock volume in the faults and increase porosity, which would enhance the detachment process. At the same time, released fluids would migrate to shallower levels along the weak zones whereby the faults could be further hydrated at shallower levels, initiating a self-weakening process. The dehydration reactions would also act if subduction initiation was induced by an external heat source such as upwelling mantle at passive margins (Gerya et al. 2015; Ueda et al. 2008; Whattam & Stern 2015). The deep hydration of transform- and passive continental/arc margin faults, shear zones and mylonitic ultramafic rocks may also provide significant amounts of the fluid volume to kick start flux melting in the early stages of subduction, which is believed to produce boninitic melts (Reagan et al. 2010; Shervais et al. 2019, 2021; Wang et al. 2020). During subduction infancy, the formation of Mg-hornblende in basal peridotites marks the beginning of mantle wedge formation and "slabitization" (Agard et al. 2020; Prigent et al. 2018). The latter authors have remarked that the exact temperature conditions of Mg-hornblende formation, i.e., fluid infiltration, cannot be assessed due to the lack of suitable thermometers in Ca-amphibole bearing peridotites. For all the geodynamic settings discussed here, we have shown, however, that the minimum temperatures for Mg-hornblende formation can be constrained between ~ 720 and 750 °C at pressures of ~ 0.3–0.8 GPa based on the detailed investigation of the Malenco contact aureole.

6 Conclusions

The Bergell contact aureole is an excellent natural laboratory to investigate dehydration reactions in serpentinized peridotites. At the north-eastern edge of the Bergell tonalite intrusion, all but Ca-amphibole dehydration reactions in natural serpentinites can be observed. In particular, within a distance of 70 m from the Bergell tonalite intrusion the three breakdown reactions forming orthopyroxene, Mg-hornblende and spinel not only ran to completion but also occurred simultaneously within a narrow temperature range of 720 ± 10 °C and a pressure of 300 ± 30 MPa. Based on the sequence of prograde reactions, a detailed temperature profile towards the Bergell intrusion was established, showing a strong increase in temperature from 520 to 800 °C within 1500 m of the contact that is inconsistent with simple heat conduction. The comparison of the established phase relations with computed phase stabilities and compositions showed that first order features are in good agreement. However, some key features, such as the appearance of Mg-hornblende and the absence of plagioclase cannot be reproduced in the calculated phase diagram sections. There are also significant differences in phase compositions, such as the Al content of chlorite and Ca-amphibole and the Mg# among the phases, indicating that quantification of fluid liberation during prograde metamorphism of serpentinites should not be based on phase diagram section computation alone.

Phase relations regarding Mg-hornblende and chlorite formation at low and high pressures were shown to be critical in a wide variety of geological settings. For example, deep serpentinization at oceanic transform- or detachment faults and de-serpentinization reactions during subduction initiation and subduction infancy all require data about low-pressure dehydration reactions in serpentinites like that obtained in this study.

Supplementary Information

The online version contains supplementary material available at https://doi.org/10.1186/s00015-022-00415-y.

Additional file 1: Figure S1. a Zone **O**: Massive olivine-antigorite serpentinite with olivine vein from Val Ventina (Euro coin 2.3 cm in diameter). **b** Plain polarised light image of olivine-serpentinite-schist from the Chiesa quarry (Sample CH_2) containing minor Cr-magnetite and relic clinopyroxene (dusty) cores which are surrounded by prograde and transparent diopside rims. **c** Crossed polarised light image of **b** showing the characteristic olivine-antigorite mosaic texture. **d** Backscatter image of Mal1101, showing the mosaic textured intergrowth of secondary clinopyroxene (diopside), olivine and antigorite. **e** Backscatter image of zoned antigorite blades and metamorphic olivine.

Additional file 2: File S1. Regional metamorphism. A short summary of the regional metamorphism in the Malenco serpentinites is presented and defined as zone **O** in the main text (see Additional file 1: Figure S1).

Additional file 3: Figure S2. a Antigorite and magnetite replacing prograde olivine along cracks (sample Ol20) in zone **III**. **b** Backscatter image

of sample Ol11b, showing mosaic textured intergrowth of olivine and pseudomorphic talc and antigorite replacement of anthophyllite.

Additional file 4: Figure S3. a Backscatter image of the olivine-orthopyroxene intergrowth in sample Ol6, zone **VI**. **b** Zoom-in of **a**, showing orthopyroxene containing the highest Al_2O_3 mass fractions reported in this study (See Additional file 11: Table S7).

Additional file 5: Table S1. Zone **O**. Quantitative EPMA analyses of olivine, antigorite, Cr-Magnetite, magnetite and clinopyroxene from samples Mal1101, CH2, Ol22 and Ol44 with the locations reported in Table 1. Mineral normalizations are given in the footnote of the table.

Additional file 6: Table S2. Zone **I&II**. Quantitative EPMA analyses of olivine, antigorite, Cr-Magnetite, magnetite and tremolite from sample Ol21 with the locations reported in Table 1. Mineral normalizations are given in the footnote of the table.

Additional file 7: Table S3. Zone **III**, Tc-in. Quantitative EPMA analyses of olivine, antigorite, Cr-Magnetite, magnetite, talc and chlorite from samples 1603 and 1604 with the locations reported in Table 1. Mineral normalizations are given in the footnote of the table.

Additional file 8: Table S4. Zone **III**. Quantitative EPMA analyses of olivine, Cr-Magnetite, magnetite, talc, chlorite and tremolite from samples Ol20, Ol18 and Ol16 with the locations reported in Table 1. Mineral normalizations are given in the footnote of the table.

Additional file 9: Table S5. Zone **IV**. Quantitative EPMA analyses of olivine, anthophyllite, Cr-Magnetite, magnetite, chlorite, tremolite, talc and antigorite from samples Ol11b and Ol11c with the locations reported in Table 1. Mineral normalizations are given in the footnote of the table.

Additional file 10: Table S6. Zone **V**. Quantitative EPMA analyses of olivine, orthopyroxene, anthophyllite, Cr-Al-spinel, Mg-hornblende, chlorite, tremolite and talc from samples Ol9 and Ol38 with the locations reported in Table 1. Mineral normalizations are given in the footnote of the table.

Additional file 11: Table S7. Zone **VI**. Quantitative EPMA analyses of olivine, orthopyroxene, anthophyllite, Cr-Al-spinel, Mg-hornblende, chlorite and tremolite from samples Ol4, Ol6 and Ol35 with the locations reported in Table 1. Mineral normalizations are given in the footnote of the table.

Additional file 12: Figure S4. Fe–Mg partitioning data from the literature using only mineral pairs within samples corresponding to the parageneses reported in this study. The black fit lines correspond with the pink fits in Fig. 10. **a** Anthophyllite: Green, purple and pink dashed lines are estimated fits from Trommsdorff and Evans (1972), Matthes and Knauer (1981) and Springer (1974) respectively. Data used to define the black line are from Springer (1974), Arai (1975), Frost (1975) and (1991). **b** Orthopyroxene: The blue regression from Trommsdorff et al. (1998) on natural data and the experimental study of Padrón-Navarta et al. (2010) coincide and define a 1:1 line, whereas the dark purple regression of Matthes and Knauer (1981) suggests a cross-over with the 1:1 line. This would indicate that at lower Mg#s than the 1:1 line, orthopyroxene shows a higher preference for Fe relative to Mg than olivine. Data for the black fit are from Springer (1974), Arai (1975), Frost (1976), Berg (1977), Pinsent and Hirst (1977), Matthes and Knauer (1981), Berg and Docka (1983) and Nozaka (2011). **c** Mg-hornblende: The pink regression line is from Springer (1974) and the black line was constructed through data of Springer (1974), Frost (1975), Frost (1976), Ashley et al. (1979) and Matthes and Knauer (1981). **d** Chlorite: Orange, blue and purple fits are from Matthes and Knauer (1981), Trommsdorff et al. (1998) and Padrón-Navarta et al. (2010) and the black line was fit through data of Arai (1975), Frost (1975), Berg (1977), Pinsent and Hirst (1977), Matthes and Knauer (1981) and Berg and Docka (1983). **e** Tremolite: The green, blue, orange and pink fits are from Trommsdorff and Evans (1972), Springer (1974), Trommsdorff et al. (1998) and Padrón-Navarta et al. (2010) and the fit through the black line through data from Rice et al. (1974), Springer (1974), Frost (1975), Berg (1977), Pinsent and Hirst (1977), Matthes and Knauer (1981), Berg and Docka (1983), Evans and Trommsdorff (1983) and Nozaka (2011). **f** Talc: Green and blue fits are from Trommsdorff and Evans (1972) and Matthes and Knauer (1981) and the black line is through data of Berg (1977), Pinsent and Hirst (1977), Matthes and Knauer (1981), Berg and Docka (1983) and Nozaka (2011).

Additional file 13: Table S8. Fe–Mg partitioning data extracted with the Perple_X subroutine Meemum for temperatures of 500, 550, 600, 650, 675, 700, 750 and 800 °C at 300 MPa. Calculated Mg#s are used in Fig. 13 and correspond with the calculated phase diagram section of Additional file 14: Figure S5.

Additional file 14: Figure S5. Pseudosection calculated with Perple_X using the 2002 revised data base of Holland and Powell (1998), augmented with Cr (Klemme et al. 2009) and corresponding solution models. Details are given in the methods and in the discussion.

Additional file 15: Figure S6. Pseudosection calculated with Perple_X using the latest Holland et al. (2018) database, Thermocalc-DS633, and corresponding solution models. Details are given in the methods and in the discussion.

Acknowledgements
We thank D. Marty, P. Manzotti and E. Gnos for editorial handling and S. Schorn and an anonymous reviewer for constructive reviews. T. Pettke provided sample Mal1101 and E. Reusser, F. Marxer, P. Ulmer and O. Müntener are thanked for valuable discussions about tonalites. H. Kempf, is gratefully acknowledged for the physically tough work and technical support he provided during the sampling campaign.

Authors' contributions
This work resulted from the PhD thesis, postdoc and freelancing of EDK. EDK conducted the fieldwork and all analytical work. Thermodynamic modelling was conceptualized by EDK and JADC. JH supervised the PhD project. EDK wrote the paper with input from all authors. All authors read and approved the final manuscript.

Funding
This work was financially supported by the Swiss National Science Foundation project 200021_169062.

Availability of data and materials
All samples, including thin and thick sections are stored at the Institute of Geological Sciences at the University of Bern, Bern, Switzerland. All data analysed during this study are included in the article and presented in Additional files 1, 2, 3, 4, 5, 6, 7, 8, 9, 10, 11, 12, 13, 14, 15: Figures S1–6, Tables S1–8 and File S1.

Declarations

Ethics approval and consent to participate
Not applicable.

Consent for publication
Not applicable.

Competing interests
The authors declare that they have no competing interests.

Author details
[1]Institute of Geological Sciences, University of Bern, Baltzerstrasse 1+3, CH-3012 Bern, Switzerland. [2]Institute of Mineralogy and Petrology, ETH Zurich, Clausiusstrasse 5, 8092 Zurich, Switzerland.

Received: 17 March 2021 Accepted: 23 February 2022
Published online: 15 April 2022

References

Agard, P., Prigent, C., Soret, M., Dubacq, B., Guillot, S., & Deldicque, D. (2020). Slabitization: mechanisms controlling subduction development and viscous coupling. *Earth–science Reviews, 208*, 1–28. https://doi.org/10.1016/j.earscirev.2020.103259

Annen, C. (2017). Factors affecting the thickness of thermal aureoles. *Frontiers in Earth Science, 5*, 82.

Arai, S. (1975). Contact metamorphosed dunite-harzburgite complex in the Chugoku district, western Japan. *Contributions to Mineralogy and Petrology, 52*(1), 1–16. https://doi.org/10.1007/BF00377998

Ashley, P. M., Ambler, E. P., & Flood, R. H. (1979). Two occurrences of ultramafic hornfels in the Biggenden Beds, southeastern Queensland. *Journal of the Geological Society of Australia: An International Geoscience Journal of the Geological Society of Australia, 26*, 29–37. https://doi.org/10.1080/00167617908729064

Batanova, V. G., Sobolev, A. V., & Kuzmin, D. V. (2015). Trace element analysis of olivine: High precision analytical method for JEOL JXA-8230 electron probe microanalyser. *Chemical Geology, 419*, 149–157.

Berg, J. H. (1977). Dry granulite mineral assemblages in the contact aureoles of the Nain complex, Labrador. *Contributions to Mineralogy and Petrology, 64*, 33–52. https://doi.org/10.1007/BF00375284

Berg, J. H., & Docka, J. A. (1983). Geothermometry in the Kiglapait contact aureole, Labrador. *American Journal of Science, 283*(5), 414–434. https://doi.org/10.2475/ajs.283.5.414

Bowen, N. L., & Tuttle, O. F. (1949). The system MgO–SiO_2–H_2O. *Geological Society of America Bulletin, 60*(3), 439–460. https://doi.org/10.1130/0016-7606(1949)60[439:TSM]2.0.CO;2

Bucher, K., & Pfeifer, H.-R. (1973). Über Metamorphose und Deformation der östlichen Malenco-Ultramafitite und deren Rahmengesteine (Prov. Sondrio, N-Italien). *Schweizerische Mineralogische Petrogrographische Mitteilungen, 53*, 231–241. https://doi.org/10.5169/seals-41383

Bucher-Nurminen, K. (1977). Die beziehung zwischen deformation, metamorphose und magmatismus im Gebiet der Bergeller Alpen. *Schweizerische Mineralogische Und Petrographische Mitteilungen, 57*, 413–434. https://doi.org/10.5169/seals-44443

Burkhard, D. J., & O'Neil, J. R. (1988). Contrasting serpentinization processes in the eastern Central Alps. *Contributions to Mineralogy and Petrology, 99*(4), 498–506. https://doi.org/10.1007/BF00371940

Chernosky, J., Day, H. W., & Caruso, L. (1985). Equilibria in the system MgO–SiO_2–$H2_O$: Experimental determination of the stability of Mg-anthophyllite. *American Mineralogist, 70*(3–4), 223–236.

Clément, M., Padrón-Navarta, J. A., & Tommasi, A. (2019). Interplay between fluid extraction mechanisms and antigorite dehydration reactions (Val Malenco, Italian Alps). *Journal of Petrology*. https://doi.org/10.1093/petrology/egz058

Connolly, J. (2009). The geodynamic equation of state: what and how. *Geochemistry, Geophysics, Geosystems,*. https://doi.org/10.1029/2009GC002540

Dale, J., Holland, T., & Powell, R. (2000). Hornblende–garnet–plagioclase thermobarometry: A natural assemblage calibration of the thermodynamics of hornblende. *Contributions to Mineralogy and Petrology, 140*(3), 353–362.

Diener, J., & Powell, R. (2012). Revised activity–composition models for clinopyroxene and amphibole. *Journal of Metamorphic Geology, 30*(2), 131–142.

Diethelm, K. H. (1985). Hornblendite und Gabbros im oestlichen Bergell (Val Sissone, Provinz Sondrio, Italien). *Schweizerische Mineralogische Und Petrographische Mitteilungen, 65*(2–3), 223–246. https://doi.org/10.5169/seals-50222

Dietrich, V. (1974). Alpine metamorphism of mafic rocks. *Schweizerisches Mineralogische Und Petrografisches Mittelungen, 54*, 291–333. https://doi.org/10.5169/seals-42197

Docka, J., Berg, J., & Klewin, K. (1986). Geothermometry in the Kiglapait aureole: Part II. Evaluation of exchange thermometry in a well-constrained thermal setting. *Journal of Petrology, 27*(3), 605–626. https://doi.org/10.1093/petrology/27.3.605

Dymkova, D., & Gerya, T. (2013). Porous fluid flow enables oceanic subduction initiation on Earth. *Geophysical Research Letters, 40*(21), 5671–5676. https://doi.org/10.1002/2013GL057798

Eberhard, L., & Pettke, T. (2021). Antigorite dehydration fluids boost carbonate mobilisation and crustal CO_2 outgassing in collisional orogens. *Geochimica Et Cosmochimica Acta, 300*, 192–214.

Eldursi, K., Branquet, Y., Guillou-Frottier, L., & Marcoux, E. (2009). Numerical investigation of transient hydrothermal processes around intrusions: Heat-transfer and fluid-circulation controlled mineralization patterns. *Earth and Planetary Science Letters, 288*, 70–83. https://doi.org/10.1016/j.epsl.2009.09.009

Eskola, P. E. (1914). On the relation between chemical and mineralogical composition in the metamorphic rocks of the Orijärvi region. *Bulletin De La Commission Géologique De Finlande, 44*, 109.

Eskola, P. E. (1921). The mineral facies of rocks. *Norsk Geologisk Tidsskrift, 6*, 143–194.

Evans, B. W. (1976). Stability of chrysotile and antigorite in the serpentine multisystem. *Schweizerische Mineralogische Und Petrographische Mitteilungen, 56*, 79–93. https://doi.org/10.5169/seals-43677

Evans, B. W., & Frost, R. B. (1976). Chrome-spinel in progressive metamorphism—a preliminary analysis. *Geochimica Et Cosmochimica Acta, 39*(6–7), 959–972. https://doi.org/10.1016/0016-7037(75)90041-1

Evans, B., & Guggenheim, S. (1988). Talc, pyrophyllite, and related minerals. *Reviews in Mineralogy, 19*, 574–587. https://doi.org/10.2138/rmg.1988.19.8

Evans, B. W., & Trommsdorff, V. (1970). Regional metamorphism of ultramafic rocks in the Central Alps: Prageneses in the system CaO–MgO–SiO_2–H_2O. *Schweizerische Mineralogische Und Petrographische Mitteilungen, 50*, 481–492. https://doi.org/10.5169/seals-39264

Evans, B. W., & Trommsdorff, V. (1978). Petrogenesis of garnet lherzolite, Cima di Gagnone, Lepontine Alps. *Earth and Planetary Science Letters, 40*(3), 333–348. https://doi.org/10.1016/0012-821X(78)90158-9

Evans, B. W., & Trommsdorff, V. (1983). Fluorine hydroxil titanian clinohumite in the Alpine recrystallized garnet peridotite: Compositional controls and petrologic significance. *American Journal of Science, 283A*, 355–369.

Ferry, J. M. (1995). Fluid flow during contact metamorphism of ophicarbonate rocks in the Bergell aureole, Val Malenco, Italian Alps. *Journal of Petrology, 36*(4), 1039–1053. https://doi.org/10.1093/petrology/36.4.1039

Floess, D., & Baumgartner, L. P. (2015). Constraining magmatic fluxes through thermal modelling of contact metamorphism. *Geological Society, London, Special Publications, 422*(1), 41–56. https://doi.org/10.1144/SP422.8

Frost, B. (1976). Limits to the assemblage forsterite-anorthite as inferred from peridotite hornfelses, Icicle Creek, Washington. *American Mineralogist, 61*(7–8), 732–750.

Frost, B. R. (1991). Introduction to oxygen fugacity and its petrologic importance. *Reviews in Mineralogy and Geochemistry, 25*, 1–9. https://doi.org/10.2138/rmg.1991.25.1

Frost, R. B. (1975). Contact metamorphism of serpentinite, chloritic blackwall and rodingite at Paddy-Go-Easy Pass, Central Cascades, Washington. *Journal of Petrology, 16*(2), 272–313. https://doi.org/10.1093/petrology/16.1.272

Fumagalli, P., & Poli, S. (2005). Experimentally determined phase relations in hydrous peridotites to 6.5 GPa and their consequences on the dynamics of subduction zones. *Journal of Petrology, 46*(3), 555–578. https://doi.org/10.1093/petrology/egh088

Fumagalli, P., Poli, S., Fischer, J., Merlini, M., & Gemmi, M. (2014). The high-pressure stability of chlorite and other hydrates in subduction mélanges: Experiments in the system Cr_2O_3–MgO–Al_2O_3–SiO_2–H_2O. *Contributions to Mineralogy and Petrology, 167*(2), 979. https://doi.org/10.1007/s00410-014-0979-5

Furlong, K. P., Hanson, R. B., & Bowers, J. R. (1991). Modeling thermal regimes. *Reviews in Mineralogy and Geochemistry, 26*(1), 437–505. https://doi.org/10.2138/rmg.1991.26.10

Gerya, T. V., Stern, R. J., Baes, M., Sobolev, S. V., & Whattam, S. A. (2015). Plate tectonics on the Earth triggered by plume-induced subduction initiation. *Nature, 527*(7577), 221–225. https://doi.org/10.1038/nature15752

Gieré, R. (1985). Metasedimente der Suretta-Decke am Ost-und Sudostrand der Bergeller Intrusion: Lithostratigraphische Korrelation und Metamorphose. *Schweizerische Mineralogische Und Petrographische Mitteilungen, 65*(1), 57–78. https://doi.org/10.5169/seals-50214

Goldschmidt, V. M. (1911). *Die Kontaktmetamorphose im Kristianagebiet* (1st ed.). Kristiania.

Goldschmidt, V. M. (1922). *Die Gesetze der Gesteinsmetamorphose mit Beispielen aus der Geologie des südlichen Norwegens* (22nd ed.). Kristiania.

Goto, A., & Tatsumi, Y. (1990). Stability of chlorite in the upper mantle. *American Mineralogist, 75*(1–2), 105–108.

Green, E., White, R., Diener, J., Powell, R., Holland, T., & Palin, R. (2016). Activity–composition relations for the calculation of partial melting equilibria in metabasic rocks. *Journal of Metamorphic Geology, 34*(9), 845–869.

Guntli, P., & Liniger, M. (1989). Metamorphose in der Margna-Decke im Bereich Piz da la Margna und Piz Fedoz (Oberengadin). *Schweizerische*

Mineralogische Und Petrographische Mitteilungen, 69(2), 289–301. https://doi.org/10.5169/seals-52795
Gyr, T. (1967). *Geologische und petrographische Untersuchungen am Ostrande des Bergeller Massivs. (Ph.D. Thesis)*. ETH Zurich.
Hansmann, W. (1996). Age determinations on the tertiary Masino-Bregaglia (Bergell) intrusives (Italy, Switzerland): A review. *Schweizerische Mineralogische Und Petrographische Mitteilungen, 76*(3), 421–451. https://doi.org/10.5169/seals-57709
Hawthorne, F. C., Oberti, R., Harlow, G. E., Maresch, W. V., Martin, R. F., Schumacher, J. C., & Welch, M. D. (2012). Nomenclature of the amphibole supergroup. *American Mineralogist, 97*(11–12), 2031–2048. https://doi.org/10.2138/am.2012.4276
Hermann, J., & Muntener, O. (1992). Strukturelle Entwicklung im Grenzbereich zwischen dem penninischen Malenco-Ultramafitit und dem Unterostalpin (Margna-und Sella-Decke). *Schweizerische Mineralogische Und Petrographische Mitteilungen, 72*, 225–240. https://doi.org/10.5169/seals-54909
Hermann, J., Müntener, O., Trommsdorff, V., Hansmann, W., & Piccardo, G. B. (1997). Fossil crust-to-mantle transition, Val Malenco (Italian Alps). *Journal of Geophysical Research, 102*(B9), 20123–20132. https://doi.org/10.3929/ethz-a-001823002
Hilairet, N., Reynard, B., Wang, Y., Daniel, I., Merkel, S., Nishiyama, N., & Petitgirard, S. (2007). High-pressure creep of serpentine, interseismic deformation, and initiation of subduction. *Science, 318*(5858), 1910–1913. https://doi.org/10.1126/science.1148494
Hirauchi, K.-I., Fukushima, K., Kido, M., Muto, J., & Okamoto, A. (2016). Reaction-induced rheological weakening enables oceanic plate subduction. *Nature Communications, 7*(1), 1–7. https://doi.org/10.1038/ncomms12550
Holland, T. J., Green, E. C., & Powell, R. (2018). Melting of peridotites through to granites: A simple thermodynamic model in the system KNCFMASHTOCr. *Journal of Petrology, 59*(5), 881–900. https://doi.org/10.1093/petrology/egy048
Holland, T., & Powell, R. (1998). An internally consistent thermodynamic data set for phases of petrological interest. *Journal of Metamorphic Geology, 16*(3), 309–343. https://doi.org/10.1111/j.1525-1314.1998.00140.x
Jaeger, J. (1961). The cooling of irregularly shaped igneous bodies. *American Journal of Science, 259*(10), 721–734. https://doi.org/10.2475/ajs.259.10.721
Jäger, E. (1973). Die alpine Orogenese im Lichte der radiometrischen Altersbestimmung. *Eclogae Geologicae Helvetiae, 66*(1), 11–21. https://doi.org/10.5169/seals-164180
Jenkins, D. M. (1981). Experimental phase relations of hydrous peridotites modelled in the system H_2O–CaO–MgO–Al_2O_3–SiO_2. *Contributions to Mineralogy and Petrology, 77*(2), 166–176. https://doi.org/10.1007/BF00636520
Jenkins, D. M. (1983). Stability and composition relations of calcic amphiboles in ultramafic rocks. *Contributions to Mineralogy and Petrology, 83*(3–4), 375–384. https://doi.org/10.1007/BF00371206
Jenkins, D. M. (1994). Experimental reversal of the aluminum content in tremolitic amphiboles in the system H_2O–CaO–MgO–Al_2O_3–SiO_2. *American Journal of Science, 294*(5), 593–620. https://doi.org/10.2475/ajs.294.5.593
Jenkins, D. M., & Chernosky, J. V. (1986). Phase equilibria and crystallochemical properties of Mg-chlorite. *American Mineralogist, 71*(7–8), 924–936.
Karig, D. E. (1982). Initiation of subduction zones: Implications for arc evolution and ophiolite development. *Geological Society, London, Special Publications, 10*(1), 563–576. https://doi.org/10.1144/GSL.SP.1982.010.01.37
Kempf, E. D., Hermann, J., Reusser, E., Baumgartner, L. P., & Lanari, P. (2020). The role of the antigorite + brucite to olivine reaction in subducted serpentinites (Zermatt, Switzerland). *Swiss Journal of Geosciences, 113*(1), 16. https://doi.org/10.1186/s00015-020-00368-0
Kerrick, D. M. (1991). Overview of contact metamorphism. *Reviews in Mineralogy and Geochemistry, 26*(1), 1–12. https://doi.org/10.2138/rmg.1991.26.1
Klemme, S., Ivanic, T., Connolly, J., & Harte, B. (2009). Thermodynamic modelling of Cr-bearing garnets with implications for diamond inclusions and peridotite xenoliths. *Lithos, 112*, 986–991. https://doi.org/10.1016/j.lithos.2009.05.007
Lafay, R., Baumgartner, L. P., Putlitz, B., & Siron, G. (2019). Oxygen isotope disequilibrium during serpentinite dehydration. *Terra Nova, 31*(2), 94–101. https://doi.org/10.1111/ter.12373
Laird, J. (1988). Chlorites; metamorphic petrology. *Reviews in Mineralogy and Geochemistry, 19*(1), 405–453.
Leake, B. E., Woolley, A. R., Arps, C. E., Birch, W. D., Gilbert, M. C., Grice, J. D., Hawthorne, F. C., Kato, A., Kisch, H. J., Krivovichev, V. G., Linthout, K., Laird, J., Mandarino, J., Maresch, W. V., Nickel, E. H., Rock, N. M. S., Schumacher, J. C., Smith, D. C., Stephenson, N. C. N., … Youzhi, G. (1997). Nomenclature of amphiboles; report of the Subcommittee on Amphiboles of the International Mineralogical Association Commission on new minerals and mineral names. *Mineralogical Magazine, 61*(405), 295–310.
Li, X. P., Rahn, M., & Bucher, K. (2004). Serpentinites of the Zermatt-Saas ophiolite complex and their texture evolution. *Journal of Metamorphic Geology, 22*(3), 159–177. https://doi.org/10.1111/j.1525-1314.2004.00503.x
Mandler, B. E., & Grove, T. L. (2016). Controls on the stability and composition of amphibole in the Earth's mantle. *Contributions to Mineralogy and Petrology, 171*(8), 1–20. https://doi.org/10.1007/s00410-016-1281-5
Matthes, S., & Knauer, E. (1981). The phase petrology of the contact metamorphic serpentinites near Erbendorf, Oberpfalz, Bavaria. *Neues Jahrbuch Für Mineralogie Abhandlungen, 141*, 59–89.
Müntener, O. (1997). *The Malenco peridotites (Alps). (Ph.D. Thesis)*. ETH Zürich.
Müntener, O., & Hermann, J. (1996). The Val Malenco lower crust–upper mantle complex and its field relations (Italian Alps). *Schweizerische Mineralogische Und Petrographische Mitteilungen, 76*(3), 475–500. https://doi.org/10.5169/seals-57711
Müntener, O., Manatschal, G., Desmurs, L., & Pettke, T. (2010). Plagioclase peridotites in ocean–continent transitions: Refertilized mantle domains generated by melt stagnation in the shallow mantle lithosphere. *Journal of Petrology, 51*(1–2), 255–294.
Mysen, B. O., & Boettcher, A. (1975). Melting of a hydrous mantle: I. Phase relations of natural peridotite at high pressures and temperatures with controlled activities of water, carbon dioxide, and hydrogen. *Journal of Petrology, 16*(1), 520–548. https://doi.org/10.1093/petrology/16.1.520
Niida, K., & Green, D. (1999). Stability and chemical composition of pargasitic amphibole in MORB pyrolite under upper mantle conditions. *Contributions to Mineralogy and Petrology, 135*(1), 18–40. https://doi.org/10.1007/s004100050495
Nozaka, T. (2011). Constraints on anthophyllite formation in thermally metamorphosed peridotites from southwestern Japan. *Journal of Metamorphic Geology, 29*(4), 385–398. https://doi.org/10.1111/j.1525-1314.2010.00921.x
Padrón-Navarta, J. A., Hermann, J., Garrido, C. J., Sánchez-Vizcaíno, V. L., & Gómez-Pugnaire, M. T. (2010). An experimental investigation of antigorite dehydration in natural silica-enriched serpentinite. *Contributions to Mineralogy and Petrology, 159*(1), 25. https://doi.org/10.1007/s00410-009-0414-5
Padrón-Navarta, J. A., Lopez Sanchez-Vizcaino, V., Garrido, C. J., & Gómez-Pugnaire, M. T. (2011). Metamorphic record of high-pressure dehydration of antigorite serpentinite to chlorite harzburgite in a subduction setting (Cerro del Almirez, Nevado-Filábride Complex, Southern Spain). *Journal of Petrology, 52*(10), 2047–2078. https://doi.org/10.1093/petrology/egr039
Padrón-Navarta, J. A., Sánchez-Vizcaíno, V. L., Hermann, J., Connolly, J. A., Garrido, C. J., Gómez-Pugnaire, M. T., & Marchesi, C. (2013). Tschermak's substitution in antigorite and consequences for phase relations and water liberation in high-grade serpentinites. *Lithos, 178*, 186–196. https://doi.org/10.1016/j.lithos.2013.02.001
Pattison, D. R. M., De Capitani, C., & Gaidies, F. (2011). Petrological consequences of variations in metamorphic reaction affinity. *Metamorphic Geology, 29*, 953–977.
Pawley, A. (2003). Chlorite stability in mantle peridotite: The reaction clinochlore+enstatite = forsterite+pyrope+H2O. *Contributions to Mineralogy and Petrology, 144*(4), 449–456. https://doi.org/10.1007/s00410-002-0409-y
Pfiffner, M. (1998). *Genese der hochdruckmetamorphen ozeanischen Abfolge der Cima Lunga-Einheit (Zentralalpen) (PhD Thesis)*. ETH Zurich.

Pinsent, R., & Hirst, D. (1977). The metamorphism of the Blue River ultramafic body, Cassiar, British Columbia, Canada. *Journal of Petrology, 18*(4), 567–594. https://doi.org/10.1093/petrology/18.4.567

Pitzer, K. S., & Sterner, S. M. (1994). Equations of state valid continuously from zero to extreme pressures for H_2O and CO_2. *The Journal of Chemical Physics, 101*(4), 3111–3116. https://doi.org/10.1063/1.467624

Pozzorini, D. (1996). *Stable isotope investigations of ophicarbonate rocks, Bergell Aureole, Valmalenco: Constraints on fluid-rock interaction. (Ph.D. Thesis)*. ETH Zurich.

Prigent, C., Agard, P., Guillot, S., Godard, M., & Dubacq, B. (2018). Mantle wedge (de) formation during subduction infancy: Evidence from the base of the semail ophiolitic mantle. *Journal of Petrology, 59*(11), 2061–2092. https://doi.org/10.1093/petrology/egy090

Prigent, C., Warren, J., Kohli, A., & Teyssier, C. (2020). Fracture-mediated deep seawater flow and mantle hydration on oceanic transform faults. *Earth and Planetary Science Letters*. https://doi.org/10.1016/j.epsl.2019.115988

Reagan, M. K., Ishizuka, O., Stern, R. J., Kelley, K. A., Ohara, Y., Blichert-Toft, J., Bloomer, S. H., Cash, J., Fryer, P., Hanan, B. B., Hickey-Vargas, R., Ishii, T., Kimura, J.-I., Peate, D. W., Rowe, M. C., & Woods, M. (2010). Fore-arc basalts and subduction initiation in the Izu-Bonin-Mariana system. *Geochemistry, Geophysics, Geosystems,*. https://doi.org/10.1029/2009GC002871

Regenauer-Lieb, K., Yuen, D. A., & Branlund, J. (2001). The initiation of subduction: Criticality by addition of water? *Science, 294*(5542), 578–580. https://doi.org/10.1126/science.1063891

Reusser, C. E. (1987). *Phasenbeziehungen im Tonalit der Bergeller Intrusion: (Graubünden, Schweiz/Provinz Sondrio, Italien). (Ph.D. Thesis)*. ETH Zurich.

Rice, J. M., Evans, B. W., & Trommsdorff, V. (1974). Widespread Occurrence of Magnesiocummingtonite in Ultramafic Schists, Cima di Gagnone, Ticino, Switzerland. *Contributions to Mineralogy and Petrology, 43*, 243–251. https://doi.org/10.1007/BF00373481

Riklin, K. (1978). Strukturen und metamorphose im Bereich der südlichen Muretto-linie. *Schweizerische Mineralogische Und Petrographische Mitteilungen, 58*, 345–356. https://doi.org/10.5169/seals-45207

Robinson, P., Spear, F. S., Schumacher, J. C., Laird, J., Klein, C., Evans, B. W., & Doolan, B. L. (1982). Amphiboles: Petrology and experimental phase relations. *Reviews in Mineralogy, 913*, 1–211. https://doi.org/10.2138/rmg.1982.10.1

Scambelluri, M., Pettke, T., Rampone, E., Godard, M., & Reusser, E. (2014). Petrology and trace element budgets of high-pressure peridotites indicate subduction dehydration of serpentinized mantle (Cima di Gagnone, Central Alps, Switzerland). *Journal of Petrology, 55*(3), 459–498. https://doi.org/10.1093/petrology/egt068

Schroeder, T., & John, B. E. (2004). Strain localization on an oceanic detachment fault system, Atlantis Massif, 30 N, Mid-Atlantic Ridge. *Geochemistry, Geophysics, Geosystems,*. https://doi.org/10.1029/2004GC000728

Shen, T., Zhang, C., Chen, J., Hermann, J., Zhang, L., Padrón-Navarta, J. A., Chen, L., Xu, J., & Yang, J. (2020). Changes in the cell parameters of antigorite close to its dehydration reaction at subduction zone conditions. *American Mineralogist, 105*, 569–582. https://doi.org/10.2138/am-2020-7159

Shervais, J. W., Reagan, M., Godard, M., Prytulak, J., Ryan, J. G., Pearce, J., Almeev, R. R., Li, H., Haugen, E., Chapman, T., Kurz, W., Nelson, W. R., Heaton, D. E., Kirchenbaur, M., Shimizu, K., Sakuyama, T., Vetter, S. K., Li, Y., Whattam, S., & Chapman, T. (2021). Magmatic response to subduction initiation, part II: Boninites and related rocks of the Izu-Bonin Arc from IOPD Expedition 352. *Geochemistry, Geophysics, Geosystems*. https://doi.org/10.1029/2020GC009093

Shervais, J. W., Reagan, M., Haugen, E., Almeev, R. R., Pearce, J. A., Prytulak, J., Ryan, J. G., Whattam, S. A., Godard, M., Chapman, T., Li, H., Kurz, W., Nelson, W. R., Heaton, D., Kirchenbaur, M., Shimizu, K., Sakuyama, T., Li, Y., & Vetter, S. K. (2019). Magmatic response to subduction initiation: Part 1. Fore-arc basalts of the Izu-Bonin arc from IODP Expedition 352. *Geochemistry, Geophysics, Geosystems, 20*(1), 314–338. https://doi.org/10.1029/2018GC007731

Springer, R. K. (1974). Contact metamorphosed ultramafic rocks in the western Sierra Nevada foothills, California. *Journal of Petrology, 15*(1), 160–195. https://doi.org/10.1093/petrology/15.1.160

Staub, R. (1921). *Über den Bau des Monte della Disgrazia* (Vol. 66). Naturforschende Gesellschaft Zürich.

Staub, R. (1946). *Geologische Karte der Bernina-Gruppe 1:50,000*. Schweizerische geologische Kommission.

Stern, R. J., & Gerya, T. (2018). Subduction initiation in nature and models: A review. *Tectonophysics, 746*, 173–198. https://doi.org/10.1016/j.tecto.2017.10.014

Stucki, A. (2001). *High grade Mesozoic ophiolites of the southern steep belt, Central Alps. (PhD thesis)*. ETH Zurich.

Tracy, R. J., & Frost, R. B. (1991). Phase equilibria and thermobarometry of calcareous, ultramafic and mafic rocks, and iron formations. *Reviews in Mineralogy, 26*, 207–289. https://doi.org/10.2138/rmg.1991.26.5

Trommsdorff, V. (1974). Alpine metamorphism of peridotitic rocks. *Schweizerische Mineralogische Petrogrographische Mitteilungen, 54*, 333–352. https://doi.org/10.5169/seals-42198

Trommsdorff, V., & Connolly, J. A. D. (1996). The ultramafic contact aureole about the Bregaglia (Bergell) tonalite: Isograds and a thermal model. *Schweizerische Mineralogische Und Petrographische Mitteilungen, 76*, 537–547. https://doi.org/10.5169/seals-57714

Trommsdorff, V., & Evans, B. W. (1972). Progressive metamorphism of antigorite schist in the Bergell tonalite aureole (Italy). *American Journal of Science, 272*(5), 423–437. https://doi.org/10.2475/ajs.272.5.423

Trommsdorff, V., & Evans, B. W. (1977). Antigorite-ophicarbonates: Contact metamorphism in Valmalenco, Italy. *Contributions to Mineralogy and Petrology, 62*(3), 301–312. https://doi.org/10.1007/BF00371017

Trommsdorff, V., & Evans, B. W. (1980). Titanian hydroxyl-clinohumite: Formation and breakdown in antigorite rocks (Malenco, Italy). *Contributions to Mineralogy and Petrology, 72*(3), 229–242. https://doi.org/10.1007/BF00376142

Trommsdorff, V., Montrasio, A., Hermann, J., Müntener, O., Spillmann, P., & Gieré, R. (2005). The geological map of Valmalenco. *Schweizerische Mineralogische Und Petrographische Mitteilungen, 85*(1), 1–13. https://doi.org/10.5169/seals-1650

Trommsdorff, V., Piccardo, G., & Montrasio, A. (1993). From magmatism through metamorphism to sea floor emplacement of subcontinental Adria lithosphere during pre-Alpine rifting (Malenco, Italy). *Schweizerische Mineralogische Und Petrographische Mitteilungen, 73*(2), 191–203. https://doi.org/10.5169/seals-55569

Trommsdorff, V., Sánchez-Vizcaíno, V. L., Gomez-Pugnaire, M., & Müntener, O. (1998). High pressure breakdown of antigorite to spinifex-textured olivine and orthopyroxene, SE Spain. *Contributions to Mineralogy and Petrology, 132*(2), 139–148. https://doi.org/10.1007/s004100050412

Trommsdorff, V., & Schwander, H. (1969). Brucitmarmore in den Bergelleralpen. *Schweizerische Mineralogische Petrogrographische Mitteilungen, 49*, 333–340. https://doi.org/10.5169/seals-38594

Trümpy, R., & Trommsdorff, V. (1980). *Alps of Eastern Switzerland, Exkurssion 4; with a contribution by S. Metzeltin*. Schweizerische Geologische Kommission, Verlag Wenk.

Ueda, K., Gerya, T., & Sobolev, S. V. (2008). Subduction initiation by thermal–chemical plumes: Numerical studies. *Physics of the Earth and Planetary Interiors, 171*(1–4), 296–312. https://doi.org/10.1016/j.pepi.2008.06.032

Ulmer, P., & Trommsdorff, V. (1999). *Phase relations of hydrous mantle subducting to 300 km* (pp. 259–281). Geochemical Society.

Van der Lee, S., Regenauer-Lieb, K., & Yuen, D. A. (2008). The role of water in connecting past and future episodes of subduction. *Earth and Planetary Science Letters, 273*(1–2), 15–27. https://doi.org/10.1016/j.epsl.2008.04.041

Vavrecka-Sidler, D. M. (1998). *Aluminium Tschermak substitution in chlorite in the system MgO–Al2O3–SiO3–H2O—a theoretical and experimental approach. (Ph.D. Thesis)*. ETH Zurich.

Vils, F., Pelletier, L., Kalt, A., Müntener, O., & Ludwig, T. (2008). The lithium, boron and beryllium content of serpentinized peridotites from ODP Leg 209 (Sites 1272A and 1274A): Implications for lithium and boron budgets of oceanic lithosphere. *Geochimica Et Cosmochimica Acta, 72*(22), 5475–5504. https://doi.org/10.1016/j.gca.2008.08.005

Vissers, R., Drury, M., Hoogerduijn, E., Spiers, C., & Van der Wal, D. (1995). Mantle shear zones and their effect on lithosphere strength during continental breakup. *Tectonophysics, 249*(3–4), 155–171. https://doi.org/10.1016/0040-1951(95)00033-J

von Blackenburg, F. (1992). Combined high-precision chronometry and geochemical tracing using accessory minerals: Applied to the

Central-Alpine Bergell intrusion (central Europe). *Chemical Geology, 100*(1–2), 19–40. https://doi.org/10.1016/0009-2541(92)90100-J
Wang, J., Takahashi, E., Xiong, X., Chen, L., Li, L., Suzuki, T., & Walter, M. J. (2020). The water-saturated solidus and second critical endpoint of peridotite: Implications for magma genesis within the mantle wedge. *Journal of Geophysical Research: Solid Earth, 125*(8), e2020JB019452.
Weiss, M. (1997). *Clinohumites: a field and experimental study. (PhD Thesis)*. ETH Zurich.
Wenk, H. R., & Cornelius, S. B. (1977). *Geologischer Atlas der Schweiz I: 25,000, Blatt No. 1296 Sciora*. Schweizerische Geologische Kommission.
Wenk, H. R., Wenk, E., & Wallace, J. H. (1974). Metamorphic mineral assemblages in pelite rocks of the Bergell Alps. *Schweizerische Mineralogische Und Petrographische Mitteilungen, 54*(2/3), 507–554. https://doi.org/10.5169/seals-42208
Whattam, S. A., & Stern, R. J. (2015). Late Cretaceous plume-induced subduction initiation along the southern margin of the Caribbean and NW South America: The first documented example with implications for the onset of plate tectonics. *Gondwana Research, 27*(1), 38–63. https://doi.org/10.1016/j.gr.2014.07.011
White, R., Powell, R., Holland, T., Johnson, T., & Green, E. (2014). New mineral activity–composition relations for thermodynamic calculations in metapelitic systems. *Journal of Metamorphic Geology, 32*(3), 261–286.
Wunder, B., Wirth, R., & Gottschalk, M. (2001). Antigorite pressure and temperature dependence of polysomatism and water content. *European Journal of Mineralogy, 13*(3), 485–496. https://doi.org/10.1127/0935-1221/2001/0013-0485

Publisher's Note

Springer Nature remains neutral with regard to jurisdictional claims in published maps and institutional affiliations.

Submit your manuscript to a SpringerOpen journal and benefit from:

► Convenient online submission
► Rigorous peer review
► Open access: articles freely available online
► High visibility within the field
► Retaining the copyright to your article

Submit your next manuscript at ► springeropen.com